THE UNIVERSITY OF CHICAGO

SEARCH FOR THE RARE DECAY $K_L^0 \to \pi^0\pi^0\nu\bar{\nu}$

A DISSERTATION SUBMITTED TO
THE FACULTY OF THE DIVISION OF THE PHYSICAL SCIENCES
IN CANDIDACY FOR THE DEGREE OF
DOCTOR OF PHILOSOPHY

DEPARTMENT OF PHYSICS

BY
YI ZHENG

CHICAGO, ILLINOIS
MARCH 2010

Dedicated to my parents, sister, wife and daughter.

TABLE OF CONTENTS

LIST OF FIGURES

LIST OF TABLES

ABSTRACT

The E391a collaboration searched for rare kaon decays at the KEK 12 GeV proton synchrotron in Tsukuba, Japan. This thesis focuses on using a blind analysis to search for the rare decay $K_L^0 \to \pi^0\pi^0\nu\bar{\nu}$. In a blind analysis, the signal region is kept hidden while choosing event selection criteria. The background was estimated through the bifurcation method to be $0.26 \pm 0.18_{stat} \pm 0.01_{syst}$. The kaon flux is estimated to be $(5.61 \pm 0.16_{stat} \pm 0.26_{syst}) \times 10^9$. After opening the box, we observed zero event. Therefore, we set an upper limit of the branching ratio of the $K_L^0 \to \pi^0\pi^0\nu\bar{\nu}$ decay at 1.1×10^{-6} at the 90% confidence level.

ACKNOWLEDGMENTS

I want to thank my parents and sister for their unselfish love and care. Their advice and encouragement have helped me go through the ups and downs of my life so far.

I am really grateful to Yau Wah for giving me this opportunity to work in this exciting kaon physics. He is a really insightful advisor, a good teacher and a sincere friend. It has been a wonderful experience to work with him.

I would also like to thank Jon Nix, Gabriel Perdue and Jiasen Ma, my office mates, for giving detailed answers to my questions about the experiment.

I also want to thank the other members of the E391a collaboration. Without them, this work would not be possible. I should also thank Risa Ogata for working with me on this decay mode.

I also thank Nobuko McNeill and David Reid for helping me go through my graduate life at University of Chicago.

Last I want to thank my wife for her encouragement and support during my years at University of Chicago.

CHAPTER 1

INTRODUCTION

The E391a experiment is the first dedicated experiment to search for the rare kaon decay $K_L^0 \to \pi^0\nu\bar{\nu}$, the "Golden Mode". The experiment has 4π hermiticity, an innovation that sets it apart from previous experiments. This thesis will focus on the search for another rare kaon decay $K_L^0 \to \pi^0\pi^0\nu\bar{\nu}$, which has four photons in the final state.

Symmetries have been one of the most fascinating aspects of physics. CPT, the combination of Charge Conjugation (C), Parity (P) and Time Reversal (T), is related to Lorentz invariance and believed to be a good symmetry. In 1956, Lee and Yang [5] first suggested that there was no evidence that P was conserved in weak interactions. In 1957, Wu [6] observed P violation experimentally. In 1964 [7], CP violation was shown to exist in kaon system. Since then, kaons have been an important field of particle physics in the study of symmetries and their violation.

1.1 Kaon Phenomenology

Kaons are mesons formed by a strange (or anti-strange) quark and an up or down quark. They have strangeness of ± 1. There are both charged kaons, K^+ and K^-, and neutral kaons, K^0 and $\bar{K}^0$. Neutral kaons are distinguished by their strangeness: $S(K^0) = 1$, $S(\bar{K}^0) = -1$. K^0 and $\bar{K}^0$ are not CP eigenstates:

$$\begin{aligned} C|K^0> &= |\bar{K}^0>, \\ C|\bar{K}^0> &= |K^0>, \end{aligned} \tag{1.1}$$

$$
\begin{aligned}
P|K^0> &= -|K^0>, \\
P|\bar{K}^0> &= -|\bar{K}^0>,
\end{aligned}
\tag{1.2}
$$

$$
\begin{aligned}
CP|K^0> &= -|\bar{K}^0>, \\
CP|\bar{K}^0> &= -|K^0>,
\end{aligned}
\tag{1.3}
$$

The following linear combinations of K^0 and $\bar{K}^0$ are CP eigenstates:

$$
\begin{aligned}
|K_1^0> &= \frac{1}{\sqrt{2}}\left(|K^0> + |\bar{K}^0>\right), \\
|K_2^0> &= \frac{1}{\sqrt{2}}\left(|K^0> - |\bar{K}^0>\right),
\end{aligned}
\tag{1.4}
$$

where $|K_1^0>$ is CP even and $|K_2^0>$ is CP odd. K_1 mainly primarily decays to 2π which occurs quickly. K_2 promarily decays to 3π which occurs on a slower timescale. Cronin and Fitch observed that CP is not conserved in weak interaction in their experiment of a decay of long lived neutral kaon to 2π [7]. The kaons observed in experiments are a mixture of K_2 with a small amount of K_1, which we call K_L [8].

1.2 Standard Model and CP Violation

In order to understand the importance of kaons and their decays, we need a basic understanding of the Standard Model. The Standard Model describes strong and electroweak interactions through gauge field theory with gauge group $SU(3) \otimes SU(2) \otimes U(1)$. Eight gluons mediate the strong interaction. $W^{\pm}$, Z^0, and γ mediate the electroweak interaction. $W^{\pm}$ can mediate flavor-changing process through the following Lagrangian:

$$
\mathcal{L} = \frac{g}{\sqrt{2}}\left[\bar{u}_i V_{ij} d_j W^- + \bar{d}_j V_{ij}^* u_i W^+\right], \tag{1.5}
$$

where V_{ij} is the *Cabibo-Kobayashi-Maskawa* matrix [9] [10], which connects the weak eigenstates (denoted with primes below) and the mass eigenstates:

$$\begin{pmatrix} d' \\ s' \\ b' \end{pmatrix} = \begin{pmatrix} V_{ud} & V_{us} & V_{ub} \\ V_{cd} & V_{cs} & V_{cb} \\ V_{td} & V_{ts} & V_{tb} \end{pmatrix} \begin{pmatrix} d \\ s \\ b \end{pmatrix} = V_{CKM} \begin{pmatrix} d \\ s \\ b \end{pmatrix} \tag{1.6}$$

The CKM matrix is unitary. Flavor changing neutral current processes are forbidden at tree level [12]. The V_{ij} may be complex, which allows CP violation in the Standard Model. The Lagrangian 1.5 tranforms under CP as below:

$$\mathcal{L} \xrightarrow[\text{CP}]{} \frac{g}{\sqrt{2}} \left[\bar{d}_j V_{ij} u_i W^+ + \bar{u}_i V_{ij}^* d_j W^- \right]. \tag{1.7}$$

If V_{ij} are not real entries,, CP will be violated.

A 3×3 unitary matrix has nine free parameters. The definition of quark phase reduced this to four. One common parameterization of CKM matrix uses three angles (θ_{12}, θ_{23}, and θ_{31}) and one phase (δ):

$$V = \begin{pmatrix} c_{12}\, c_{13} & s_{12}\, c_{13} & s_{13}\, e^{i\delta} \\ -s_{12}\, c_{23} - c_{12}\, s_{23}\, s_{13}\, e^{i\delta} & c_{12}\, c_{23} - s_{12}\, s_{23}\, s_{13}\, e^{i\delta} & s_{23}\, c_{13} \\ s_{12}\, c_{23} - c_{12}\, s_{23}\, s_{13}\, e^{i\delta} & -c_{12}\, c_{23} - s_{12}\, s_{23}\, s_{13}\, e^{i\delta} & c_{23}\, c_{13} \end{pmatrix} \tag{1.8}$$

where c_{ij} is $\cos(\theta_{ij})$ and s_{ij} is $\sin(\theta_{ij})$. s_{13} and s_{23} are $\sim 10^{-3}$. As a good approximation, $c_{13} = c_{23} = 1$. Then we have $s_{12} = |V_{us}|$, $s_{13} = |V_{ub}|$, $s_{23} = |V_{cb}|$, and δ as the four independent parameters. This is the so-called "standard" parameterization and is quite useful for numerical computations. The disadvantage is that it does not clearly

show the internal structure in the parameters.

Another famous parameterization due to Wolfenstein [11] reveals the internal structure. It is an expansion of $\lambda = |V_{us}| \approx 0.22$:

$$V = \begin{pmatrix} 1 - \lambda^2/2 & \lambda & A\,\lambda^3\,(\rho - i\,\eta) \\ -\lambda & 1 - \lambda^2/2 & A\,\lambda^2 \\ A\,\lambda^3\,(1 - \rho - i\,\eta) & -A\,\lambda^2 & 1 \end{pmatrix} + \mathcal{O}(\lambda^4) \tag{1.9}$$

This parameterization is not unitary, which means higher order terms in λ must be included to provide consistent calculations.

Unitarity of the CKM matrix requires:

$$V_{ud}V_{us}^* + V_{cd}V_{cs}^* + V_{td}V_{ts}^* = 0, \tag{1.10}$$

$$V_{us}V_{ub}^* + V_{cs}V_{cb}^* + V_{ts}V_{tb}^* = 0, \tag{1.11}$$

$$V_{ud}V_{ub}^* + V_{cd}V_{cb}^* + V_{td}V_{tb}^* = 0, \tag{1.12}$$

The requirement can be represented by a triangle in the complex plane. To an excellent approximation,$V_{cd}V_{cb}^* = -A\,\lambda^3 + \mathcal{O}\left(\lambda^7\right)$ is real. If we rescale Equation 1.12 by $1/(A\,\lambda^3)$, the three terms can be represented by three vectors in the complex plane. The three vectors form a triangle as illustrated in Figure 1.1. The height of the triangle is $\bar{\eta}$ ($\bar{\eta} = \eta\left(1 - \frac{\lambda^2}{2}\right)$) and the horizontal position of the vertex is given by $\bar{\rho}$ ($\bar{\rho} = \rho\left(1 - \frac{\lambda^2}{2}\right)$).

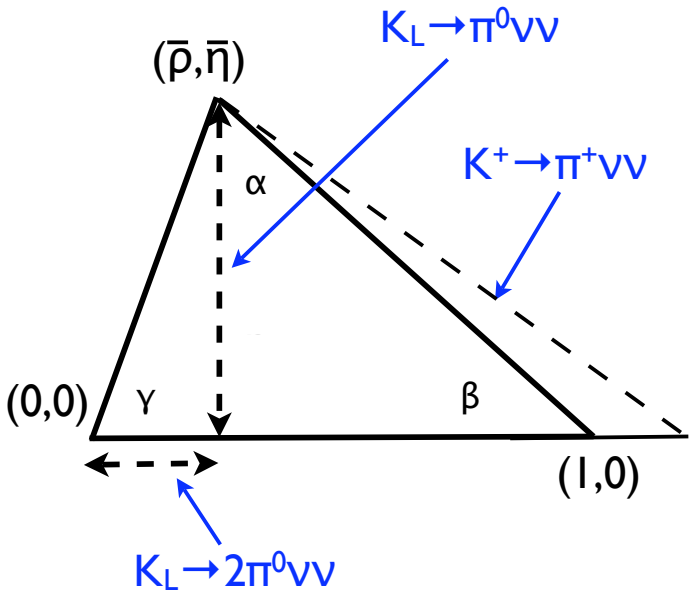

Figure 1.1: The Unitarity Triangle with the impacts of different decay modes on the parameters.

1.3 $K_L^0 \to \pi^0\pi^0\nu\bar{\nu}$ Decay and its Theoretical Predictions

$K_L^0 \to \pi^0\pi^0\nu\bar{\nu}$ is predicted to exist in the Standard Model. Figure 1.2 shows the Feynman diagrams that contribute to the decay. Its branching ratio is proportional to ρ^2 in the CKM matrix, which can determine the horizontal position of the vertex of the unitarity triangle. As a flavor changing neutral current process, it is sensitive to loop processes and not the tree-level. Thus its branching ratio are sensitive to new particles in the loop that must be summed over. It provides a great way to test the Standard Model and its extensions. It is also quite complementary to experiments at the Tevatron or the Large Hadron Collider (LHC) which may be able to find signatures of new physics. As a fully neutral mode, it is not sensitive to long range interactions. Its branching ratio can be predicted with little theoretical uncertainty. The discussion follows [1] and the more recent prediction [2].

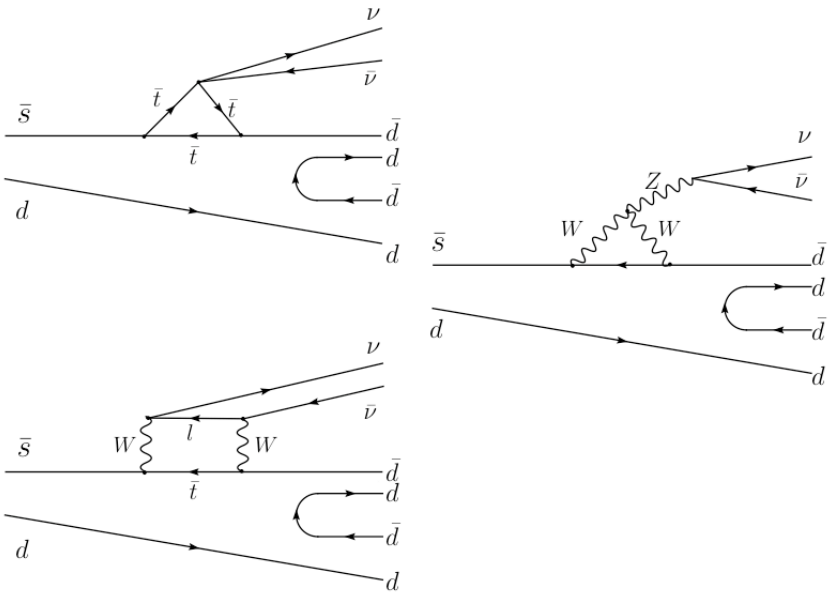

Figure 1.2: The Feynman diagrams that contribute to $K_L^0 \to \pi^0\pi^0\nu\bar{\nu}$.

The effective Lagrangian is

$$\mathcal{L} = \frac{G_F}{\sqrt{2}} \frac{\alpha}{2\pi \sin\theta_W^2} \left[V_{cs}^* V_{cd} \bar{X}(x_c, y_l) + V_{ts}^* V_{td} X(x_t)\right] \times \bar{s}\gamma_\mu(1-\gamma_5)d\bar{\nu}\gamma^\mu(1-\gamma_5)\nu + H.c. \tag{1.13}$$

where the dependence on the top-quark, charm-quark and tau-lepton masses is contained in functions $X(x_t)$ and $\bar{X}(x_c, y_l)$ through $x_i = M_i^2/M_W^2$ and $y_l = m_l^2/M_W^2$

$$X(x_t) = \frac{x_t}{8}[\frac{x_t+2}{x_t-1} + \frac{x_t-2}{(x_t-1)^2}\log x_t]. \tag{1.14}$$

The functional form of $\bar{X}(x_c, y_l)$ can be found in [3].

The calculation of the branching ratio depends on the matrix element for the hadronic current. The hadronic matrix elements relevant to $K_L^0 \to \pi^0\pi^0\nu\bar{\nu}$ can be related to those of $K^+ \to \pi^0\pi^0 e^+\nu$ through isospin symmetry:

$$< \pi^0\pi^0|(\bar{s}d)_{V-A}|K^0 > = < \pi^0\pi^0|(\bar{s}u)_{V-A}|K^+ > . \tag{1.15}$$

The most recent prediction of the branching ratio is [2]:

$$Br(K_L \to \pi^0\pi^0\nu\bar{\nu}) = (1.4 \pm 0.4) \times 10^{-13}. \tag{1.16}$$

When physics beyond standard model is considered, the branching ratio can go up to 1.0×10^{-12}.

Because $K_L^0 \to \pi^0\pi^0\nu\bar{\nu}$ has a vector matrix element, the decay is different from a pure phase space decay and is described by a form factor. Details of the form factor can be found in [21].

CHAPTER 2

THE E391A EXPERIMENT

2.1 Important Features

The E391a is the first dedicated experiment in search of the "Golden Mode", $K_L^0 \to \pi^0\nu\bar{\nu}$. The collaboration has eleven institutes from five countries, Japan, United States, Russia, Korea and Taiwan. The experiment was done in Japan at KEK.

The experiment had three runs. Run I was from the beginning of February 2004 to the middle of July 2004. Run II started in February 2005 and ended in April 2005. Run III started in October 2005 and ended in December 2005. This thesis will focus on Run II for the decay $K_L^0 \to \pi^0\pi^0\nu\bar{\nu}$. Run I results were published [4], which set the first upper limit of 4.7×10^{-5} at the 90% C.L.

The innovation of the experiment is using full 4π hermetic photon veto coverage and a tightly collimated beam to secure the P_T resolution. Thus no charged tracking apparatus was used. The trigger rate is about 200 Hz, 400 triggers in a 2 second on, 2 second off beam spill. Photon identification is handled through a CsI inorganic crystal scintillator array with photon position resolution on the order of 1 cm and energy resolution (σ/μ) of $\sim 1\% \oplus 1\%/\sqrt{E}$, where E is measured in GeV. The final state of $K_L^0 \to \pi^0\pi^0\nu\bar{\nu}$ has four photons with missing transverse momentum (P_T) and missing mass (the invariant mass of the four photons). Thus the basic approach is to look for four photons in the CsI calorimeter with no signal in any veto detectors.

The CsI calorimeter is required to have good position and energy resolution. Since the vetoes are used to reject events with any sort of hit outside the CsI calorimeter, their performance requirements are somehow looser.

2.2 Beam Line

The E391a beamline was designed mainly for the search of $K_L^0 \to \pi^0\nu\bar{\nu}$. The lessons from the KTeV experiment are that the beam halo (the tail of the radial distribution of beam density) must be highly suppressed and the beam should be narrow and well collimated to minimize the transverse momentum of kaons, which requires a "pencil" beam. There is a trade-off with the overall flux, but the general idea is to fix the decay vertex in $X - Y$ space as best as possible.

The E391a beam is produced by 12 GeV protons striking a platinum target. The target is 60 mm thick (0.68 interaction lengths) and 8 mm in diameter. The beam line is extracted at 4^0 angle with respect to the main proton beam. From peak-to-halo, the beam intensity dropped by almost five orders of magnitude, with the bulk of the beam within 1-2 cm of the nominal beam axis, as shown in Figure 2.1.

We also sought to maximize the fraction of the beam composed of actual K_L^0's. Stray neutrons and photons, not electrically charged, are difficult to remove from the beam. They can pose serious problems, by either creating accidental false veto events and decreasing acceptance or by faking the signature for $K_L^0 \to \pi^0\pi^0\nu\bar{\nu}$.

There are six collimators, labeled C1 through C6 in order away from the target, a pair of sweeping magnets, and two absorbers (one lead (Pb) and one beryllium (Be)). These components are shown in Figure 2.2.

The functions of the main components of the beam are (from [13]):

1. The beam-line is extracted at an angle of four degrees with respect to the primary proton beam, producing kaons with a mean momentum of 3.5 GeV/c at the target.

2. The beam-line is 10 m in length to reduce the hyperon and K_S content of the

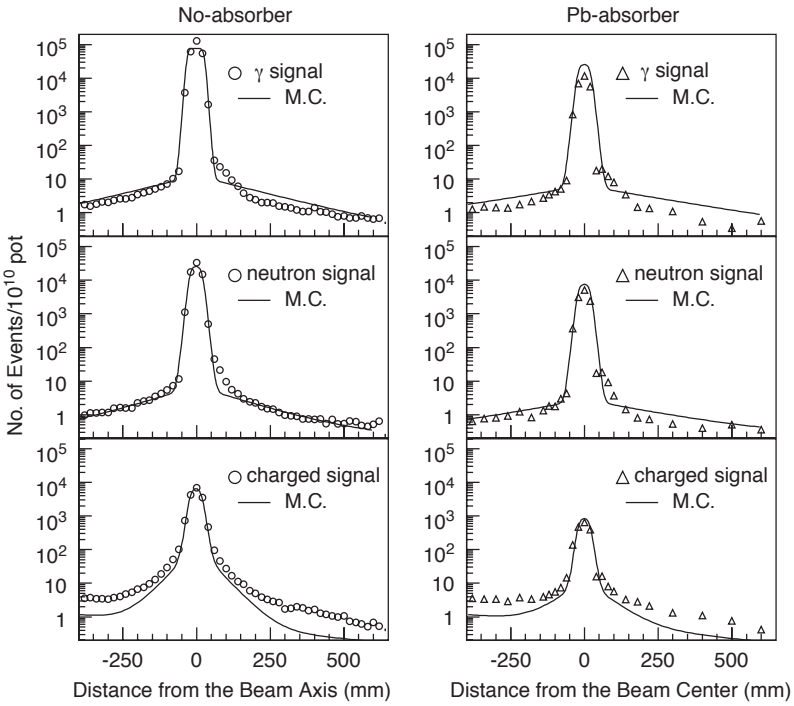

Figure 2.1: The K^0 beam-line peak-to-halo comparisons for different beam products, reproduced from [13].

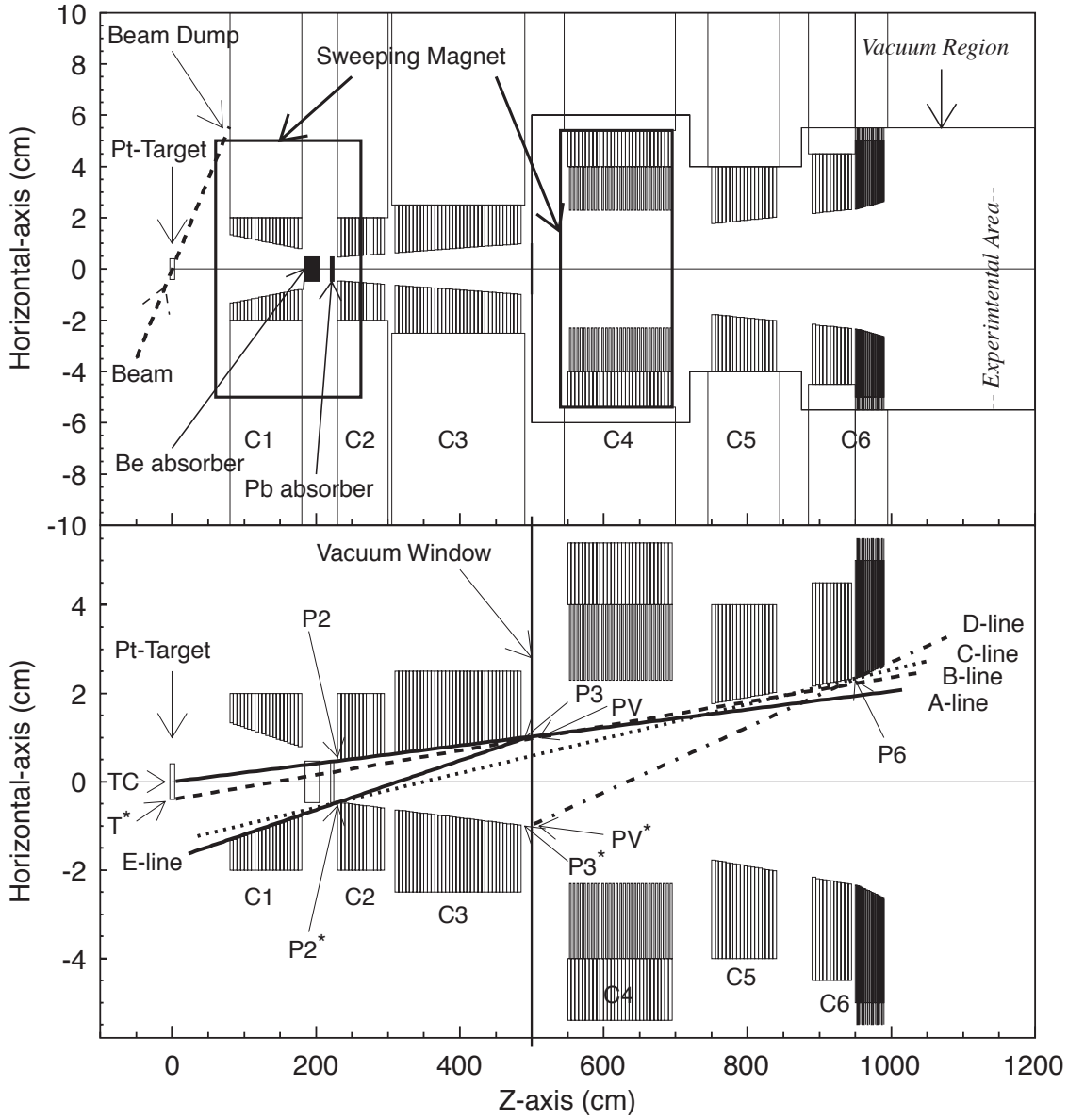

Figure 2.2: The K^0 beam-line for E391a, reproduced from [13]. The top of the figure shows the sizes and positions of the components (note the different vertical and horizontal scales), and the bottom of the figure details the collimation scheme.

beam to negligible levels. With the full detector installed, the target was 11 m from the beginning of the detector.

3. Collimators C1, C2 and C3 are used to define the beam profile, half-cone angle of 2 mrad.

4. Collimators C5 and C6 are used to trim the beam halo. Collimator C6 has an active component (plastic scintillator) to veto background events generated in collimator interactions (this veto turned out to be unnecessary).

5. One of the middle collimators (C4) contained thin Gd_2O_3 sheets to reduce the low energy thermal neutron content of the beam.

6. Two dipole magnets are deployed to sweep charged particles from the beam.

7. Two in-beam absorbers are available to reduce photon and neutron components of the beam. During Run II physics data-taking, we used both absorbers. One absorber was a 7 cm thick block of lead with high Z to reduce the photon content of the beam. The other was a 30 cm block of beryllium with low Z to reduce the neutron component. Reducing the photon content of the beam was particularly important for the functioning of the last veto, the Beam-Anti. After analyzing our results from Run I, which was conducted with the lead absorber only, we decided to also use the beryllium absorber to reduce the neutron backgrounds in exchange for a small sacrifice in flux (the absorber also reduces the kaon content of the beam).

8. The air pressure in the second half of the beam-line was lowered to the one pascal level, and separated from the fiducial decay region by a thin membrane. (The

air pressure of the fiducial decay region was held at 10^{-5} Pa during physics data taking.)

2.2.1 Proton Synchrotron

The total extraction cycle was four seconds. Over the course of the first two seconds, protons were accelerated in the proton synchrotron (PS) to a kinetic energy of 12 GeV. During the next two seconds, the protons were extracted to the KEK East Hall where they would strike a platinum (Pt) target at an angle of four degrees with respect to the E391a beam line. Typical proton intensities ranged from 2×10^{12} to 3×10^{12} protons per spill. A four degree extraction angle was chosen to minimize the neutron to kaon ratio. We achieved a n/K ratio of about 60. Further details on the synchrotron are available in [14].

2.2.2 Running Conditions

A number of beam quality cuts were employed to get the good quality data. These quality cuts included: Secondary Emission Counter (SEC) values, online veto stability, accelerator stability and pedestal stability. We required the SEC count to be within a range around the empirical values observed during ideal beam conditions. Individual runs and spills taken when the accelerator failed were removed along with runs that showed poor veto system behavior for various reasons in the online monitor plots. In total, we collected 1.4×10^{18} protons on target (POT) in the physics runs.

2.3 Detector Overview

Figure 2.3 shows the coordinate system used relative to each sub-detector. Figure 2.4 provides a sense of scale relative to human size.

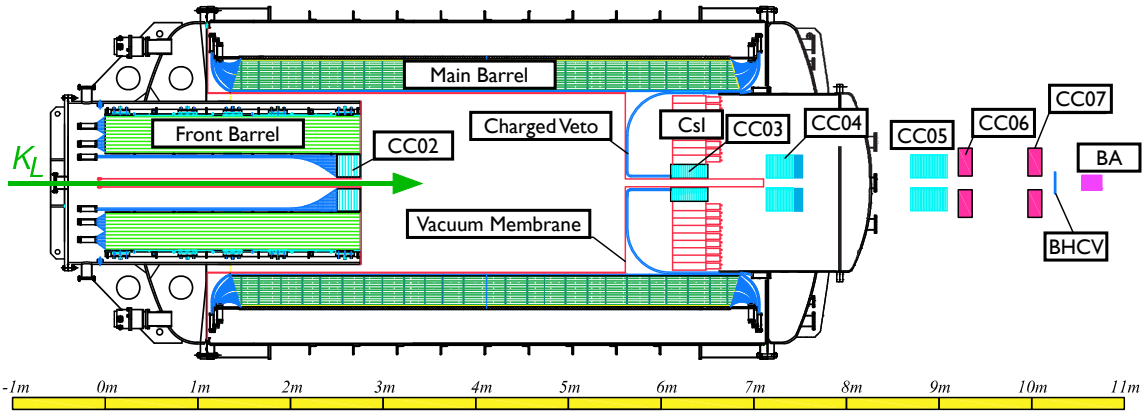

Figure 2.3: The E391a Detector is shown in plain view with a numeric length scale. The origin of our coordinate system is at the beginning of the Front Barrel. In our right-handed coordinate system, the z-axis points downstream and the y-axis points vertically upwards.

The most important piece of the detector is the cesium iodide (CsI) inorganic crystal array. This crystal array forms the calorimeter and is used for event reconstruction. The CsI array was placed at the downstream end of a lead-scintillator sandwich barrel veto called the Main Barrel (MB). In front of this large barrel veto we placed a smaller barrel veto, the Front Barrel (FB). The purpose of MB and FB was to capture photons that missed the CsI array. At the end of the beam line we placed a Beam-Anti veto (BA) to capture photons that escaped down the beam hole. Because the BA was exposed directly to the beam, it had to be sensitive to accidental losses due to interactions with beam neutrons. The beam axis was surrounded with a set of collar vetoes (referred to as collar counters) to reject beam halo interactions, very backwards and forward going

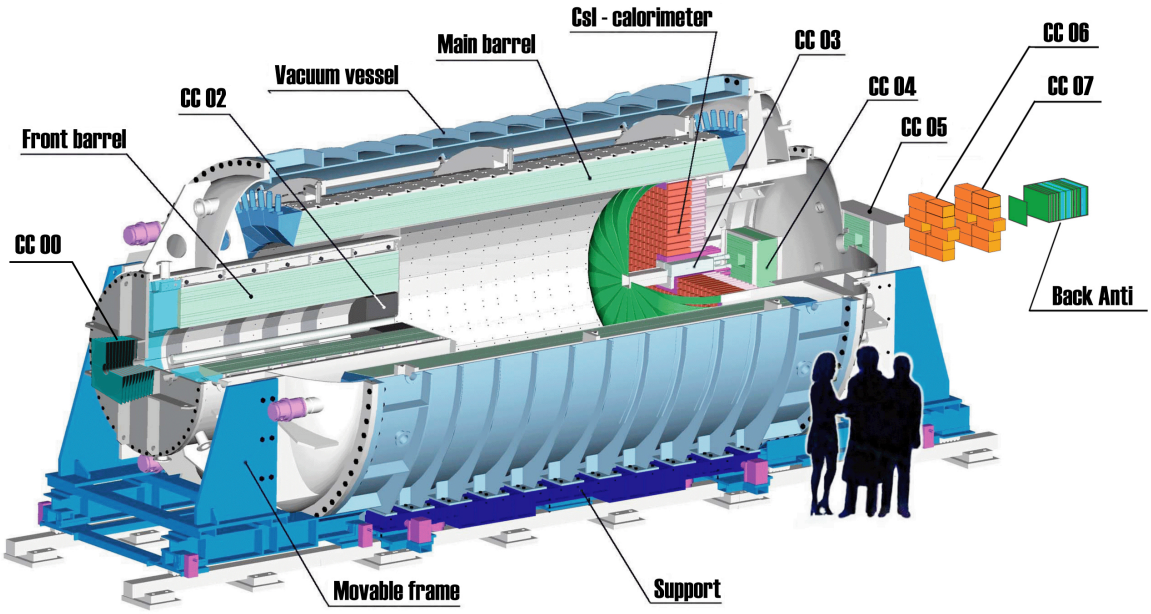

Figure 2.4: The E391a Detector is shown with human figures for scale.

daughter particles of kaon decays. Some of these collar counters were located to cover any remaining uncovered escape phase space for kaon decay products and ensure 4π hermeticity.

2.4 Front Barrel

The Front Barrel (FB) is a lead-scintillator sandwich detector. It is located upstream of the main decay volume. The FB is 17.5 X_0 (radiation length) thick transverse to the beam and made of sixteen modules. For each module, it was read out from the upstream end using two PMT's, one for inner layer and one for outer layer. The downstream ends of the optical fibers are covered with aluminized mylar to minimize light loss.

The FB was calibrated using tracks built off a trigger in the MB, with coincidence

with CC02 required. Energy deposition in the barrel was defined using normalization by data from the downstream end of the barrel.

2.5 Main Barrel

The Main Barrel (MB) is a lead-scintillator sandwich detector that is 13.5 X_0 thick. It was designed to reject kaon backgrounds that contain spare photons missing the CsI calorimeter in the transverse direction. MB overlaps with the end of the Front Barrel and the beginning of the CsI array and surrounds the decay region. The MB is 5.5 m long on the beam axis, with an inner diameter of 2 m and an outer diameter of 2.76 m. Figure 2.5 shows how the MB fits inside its container. Because MB covered a large area, it is the most important sub-detector after the CsI.

The MB was made of 32 trapezoidal modules. See Figure 2.6 for a diagram of a single module, viewed from the end. The modules were arranged around the beam axis so as to present no holes or cracks to outward rays from the beam axis. Each module was read out by four PMTs - two from each end. Internally, each module was made of two pieces, an inner piece and an outer piece. The inner and outer segments were read out by different PMTs (one at each end of the segment). The inner module was made of fifteen 1 mm lead and 5 mm scintillator layers. The outer module was built from thirty 2 mm lead and 5 mm scintillator layers.

The MB was calibrated primarily using cosmic rays. Both the gain of each part of each module and the timing information were computed by applying coincidence triggers to opposing modules. Because high statistics were required for the calibration, we took cosmic runs whenever the beam was off. Long cosmic runs were also taken before and after each of the three main Runs of E391a.

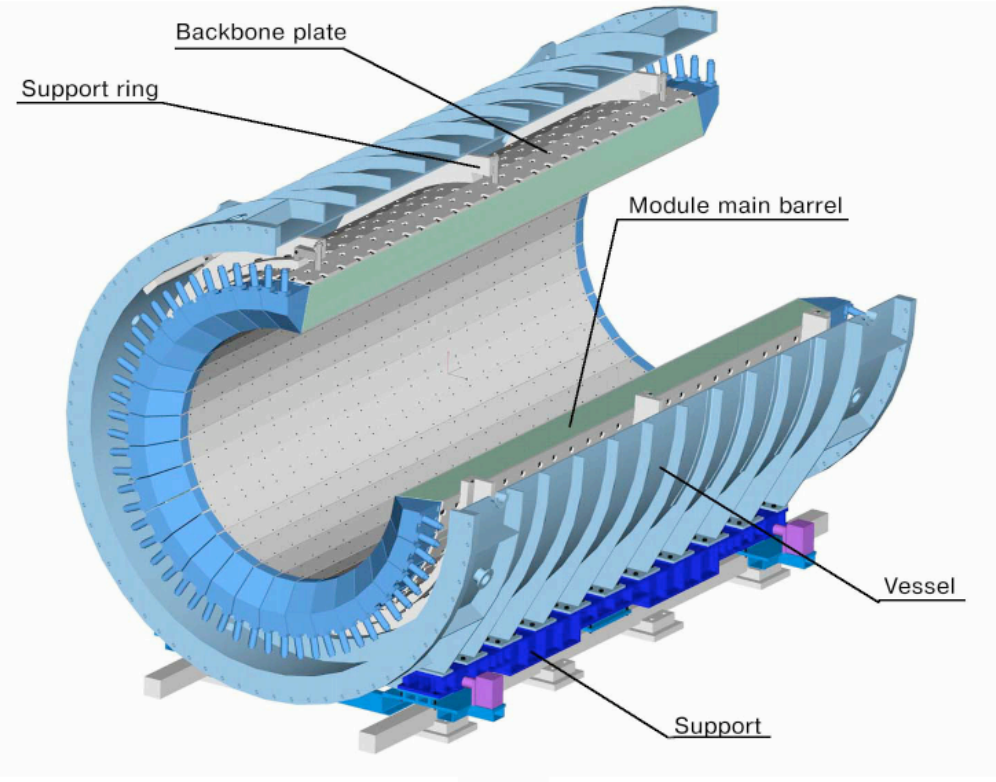

Figure 2.5: The Main Barrel.

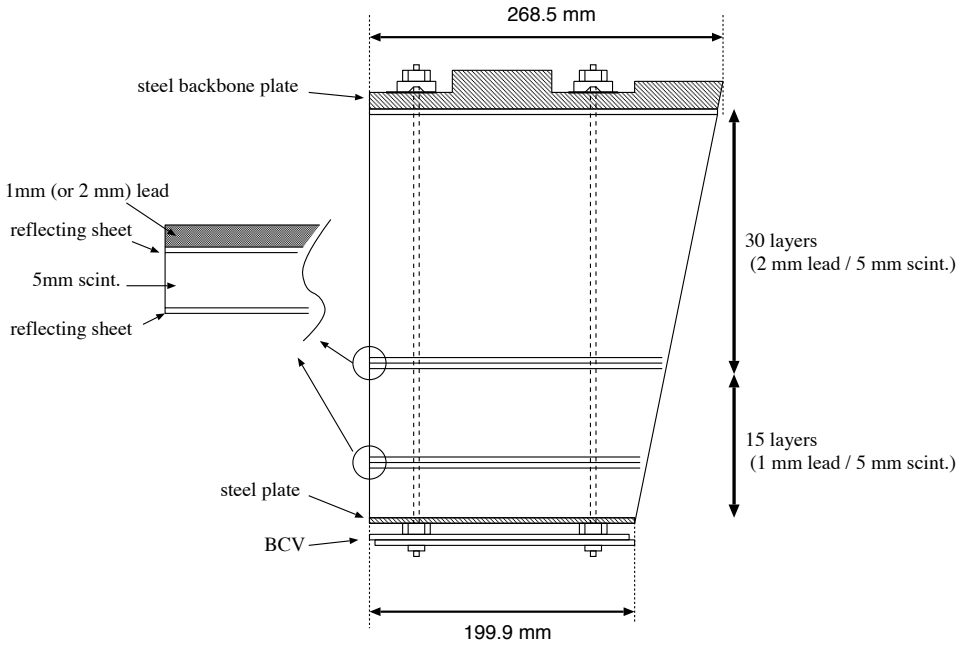

Figure 2.6: A single Main Barrel module.

2.6 Barrel Charged Veto

The Barrel Charged Veto (BCV) was placed within the inner radius of the MB because of the high probability of a kaon decay producing a charged particle. The BCV was made of thirty-two segments, offset slightly from direct alignment with each corresponding MB module. Each panel of the BCV was made from two 5 mm thick pieces of scintillator, each 550 cm long. Wavelength-shifting (WLS)fibers were glued into grooves between each pair of plates with optical cement and read into PMTs, with one PMT placed at both the up and downstream ends of each module of the BCV.

2.7 Collar Counters

There were seven Collar Counters, CC00, CC02-07. CC01 was originally included in the design, but later removed [15]. The purpose of the Collar Counters was to veto particles escaping from the main volume with trajectories near the beam axis. Most of the Collar Counters were calibrated using beam muons. It was possible to form coincidence triggers with CC00, CC02, and CC04-07. CC03 was calibrated using cosmic rays, because of the orientation of its scintillator.

CC00 is a tungsten-scintillator sandwich detector installed around the beam-pipe and outside the vacuum region after Run I. The purpose is to reduce the neutron content in the beam halo with an active detector element.

CC02 is a shashlik style lead-scintillator sandwich veto. In a typical lead-scintillator sandwich detector, light is extracted by optical fibers placed in grooves running parallel to the plane of the scintillator. Because CC02 was inside FB, this was not possible for CC02. The probability of interaction between a particle and scintillator plates would be increased if the lead and scintillator plates were perpendicular to the beam direction. For this reason, light was extracted from CC02 using optical fibers that were inserted in holes drilled into the lead and scintillator sheets such that the fibers passed perpendicular to the material planes. See Figure 2.7 for lay out of the module.

CC03 is a sandwich detector composed of tungsten-scintilator modules with traditional fiber readout parallel to the plates. The planes of the material in CC03's modules are parallel to the beam. See Figure 2.8. CC03 was calibrated using cosmic ray muons.

CC04 is a lead-scintillator sandwich detector sitting inside the vacuum vessel behind the CsI array. CC05 is also a lead-scintillator sandwich detector, but is is located

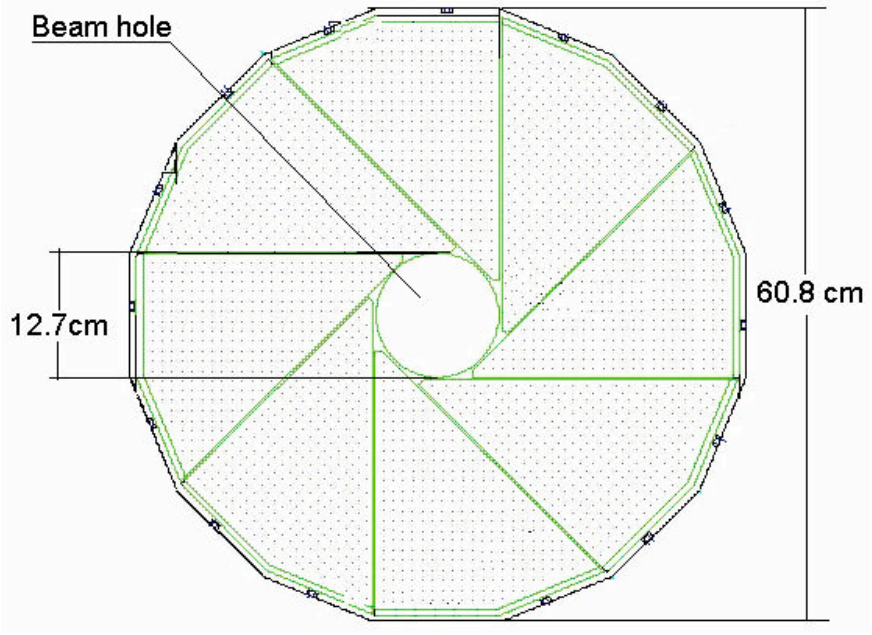

Figure 2.7: CC02, shown here looking downstream (the beam would pass through the center gap region).

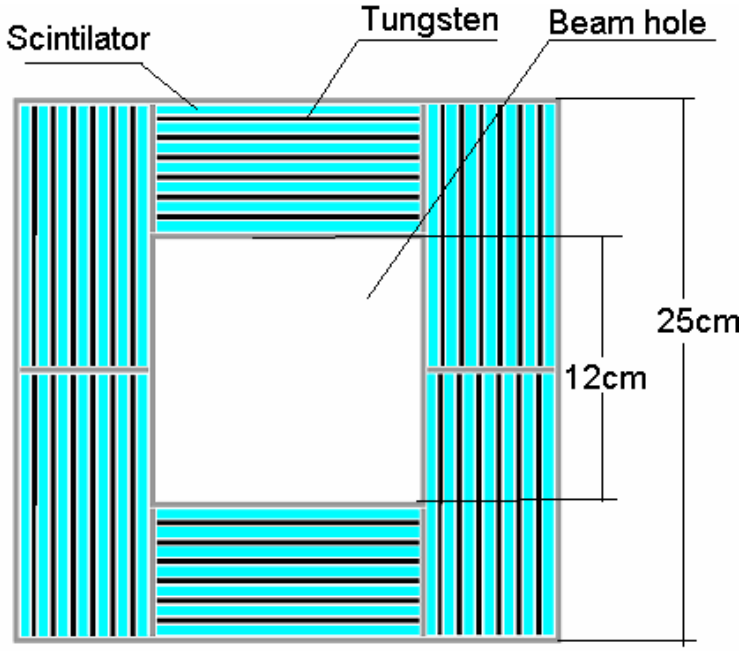

Figure 2.8: CC03 as seen looking down the beam axis.

outside the vacuum vessel and downstream of CC04. They are both 40×40 cm^2 in area on the front face, with 6.2×6.2 cm^2 square apertures in their centers for the vacuum beam pipe. Both CC04 and CC05 have charged veto and calorimetric sections. CC04 has only one charged layer on the upstream face of the detector, while CC05 has two charged-veto layers with one on the upstream face and one on the downstream face. Thus CC04 has four channels and CC05 has six channels.

CC06 and CC07 are almost the same in terms of internal structures. They were each made of ten blocks of $15 \times 15 \times 30$ cm^3 lead-glass. Figure 2.9 shows how they were designed. CC06 was initially intended to protect a very small piece of the 4π hermetic coverage. CC07 was designed to protect against the back-splash from BA.

2.8 Charged Veto

A large fraction of the decay modes of K_L^0, such as $K_L^0 \to \pi^+\pi^-\pi^0$, $K_L^0 \to \pi^\pm e^\mp \nu$ and $K_L^0 \to \pi^\pm \mu^\mp \nu$, can produce charged particles. Therefore, a charged veto was used to protect our CsI calorimeter against backgrounds associated with charged decay modes of K_L^0. The Charged Veto was made of Outer Charged Veto and Inner Charged Veto. The Outer Charged Veto consisted of thirty-two panels. Those panels overlapped with each other. They extended from the face of the CsI and was read out at the far edges of the CsI. The Inner Charged Veto consisted of four panels positioned inside CC03 and were read out through the back of the array. Each panel was read into a two inch Hamamatsu R329 PMT. Figure 2.10 shows the configuration of the panels.

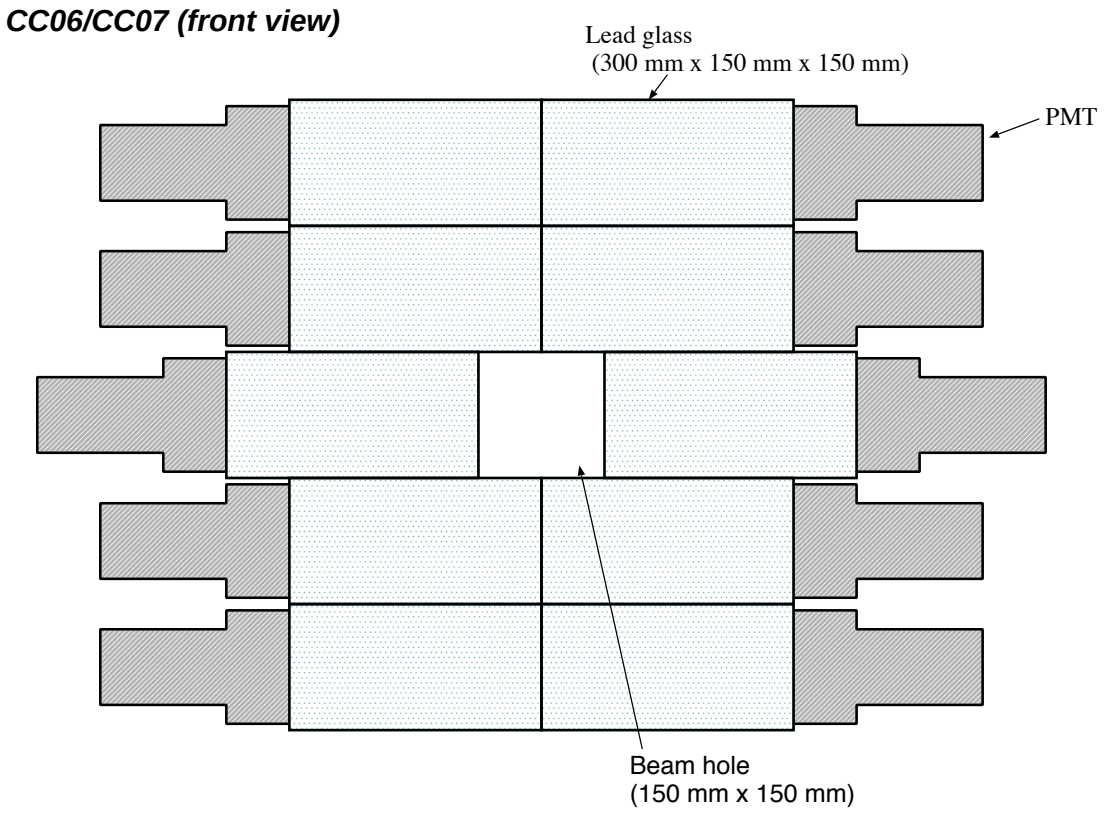

Figure 2.9: CC06/CC07 - both detectors were constructed identically out of lead-glass blocks.

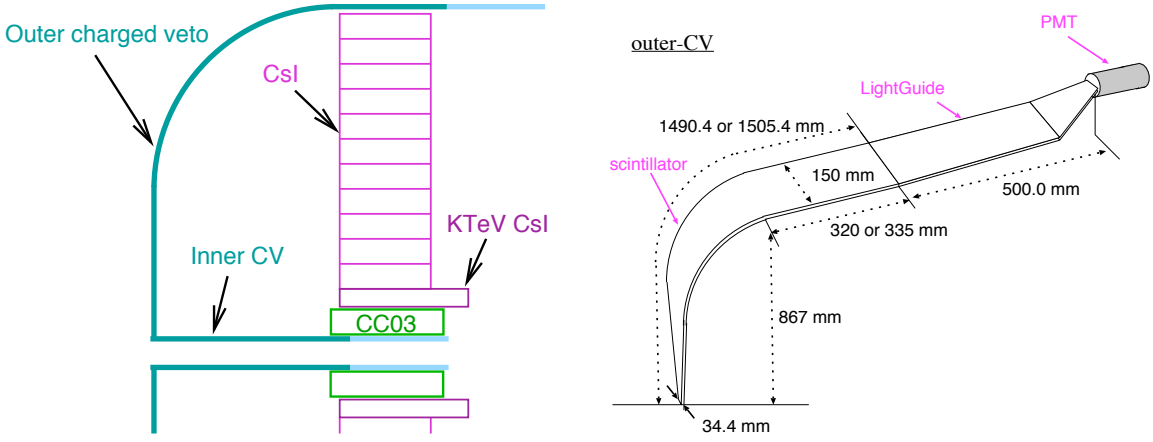

Figure 2.10: The Outer Charged Veto.

2.9 CsI Calorimeter

The main electromagnetic calorimeter was made of 576 Cesium-Iodide (CsI) crystals. 496 of them were borrowed from a previous experiment at KEK and were 7 cm $\times$ 7 cm $\times$ 30 cm (about 16 X_0). The innermost part of the array was built from 24 crystals that were 5 cm $\times$ 5 cm $\times$ 50 cm (about 27 X_0). Those crystals were borrowed from the KTeV experiment at Fermi National Accelerator Laboratory (FNAL). Regular crystals cannot fit into the outer edge of the array. So deformed CsI crystals and lead-scintillator sandwich counters were used for the outer edge of the array. The deformed CsI blocks were read out individually and used in photon clustering and as veto counters in exactly the same way as the rest of the CsI. The sandwich counter modules are triangular. The lead and plastic scintillator plates were oriented parallel to the beam. There were a total of twenty-four such counters. They were grouped into eight groups of three for readout purposes. Figure 2.11 shows the deformed CsI and lead-scintillator sandwich counters.

The usual KEK CsI crystals were each wrapped in 100 micron thick teflon sheets and 20 micron thick aluminized mylar sheets for optical isolation. The average light yield for one crystal was 15 photo-electrons per MeV. Each crystal was attached to a 2-inch Hamamatsu R4275-02 PMT. The PMTs were operated in vacuum. A cooling and temperature stability system was designed for this reason [14] [17]. The KTeV crystals were wrapped using 13 micron thick mylar sheets, with reflective coating placed to smooth the light yield across each crystal. Each crystal was attached to a 1.5-inch Hamamatsu R580-UV PMT.

The sandwich counters were used as veto. They were read out using wavelength-shifting (WLS) fibers glued into grooves in the scintillator. The fibers were terminated

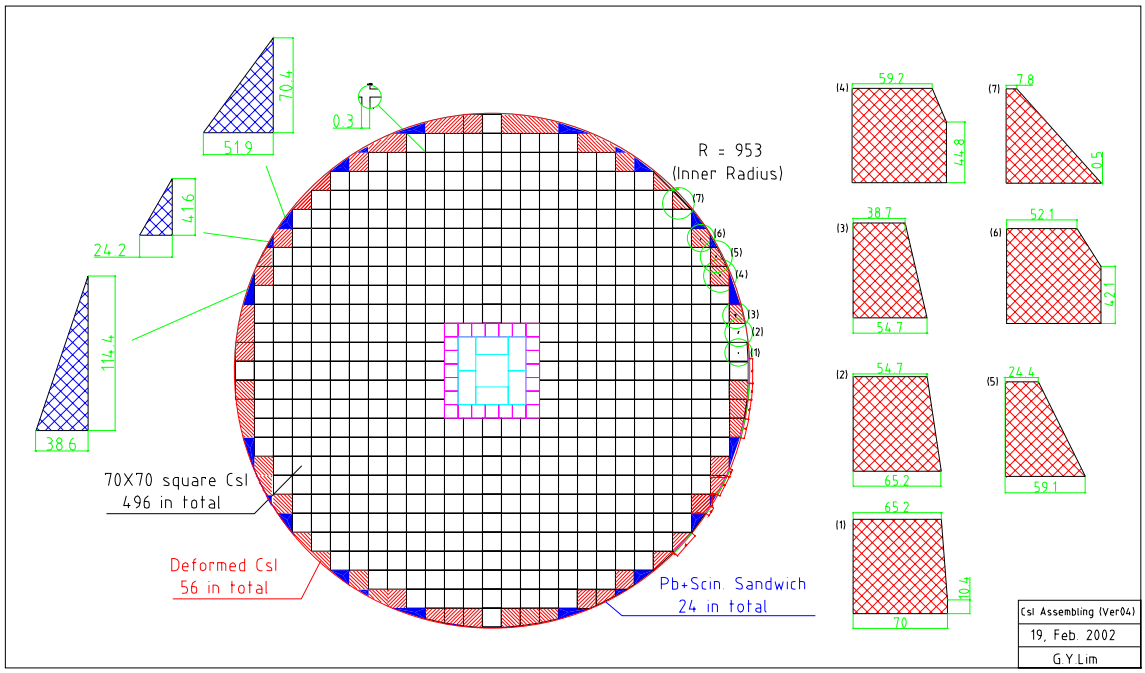

Figure 2.11: The deformed CsI and lead-scintillator sandwich counters in the outer edge of the CsI array.

in 1.125-inch Hamamatsu H1398 PMTs. Light yields were 10 to 20 photoelectrons per MeV. Figure 2.12 shows the design of the sandwich counter module.

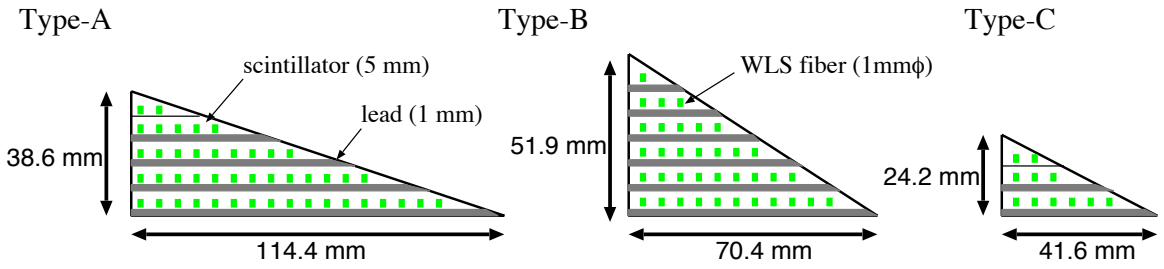

Figure 2.12: The design of sandwich counter modules.

The gain of the CsI crystals was monitored on a spill-by-spill basis using a Xenon flasher monitoring system. See references [14] and [17] for detailed information on this system. The calibration of the CsI main calorimeter is very important and will be discussed separately in a later section.

2.10 The Back-Anti (BA)

The final version of the Back-Anti (BA) used in Run I and Run II was designed by the Chicago Group. A different version of the BA was used for Run III as a test for future experiment. Figure 2.13 shows the BA used in Run II.

The BA and the Beam-Hole Charged Veto (BHCV) were calibrated using muons produced by closing the beam shutter. Because there were no other detectors that could be used to create a coincidence with the BA, the BA-BHCV muon trigger was a self-trigger made between the first and last scintillator layers. Between each muon run there was measurable PMT fatigue, which made calibration difficult. Additionally, there was difference in effective gains between on-spill and off-spill. The low intensity muon-run can well reproduce the off-spill gain, but we need on-spill gain for physics

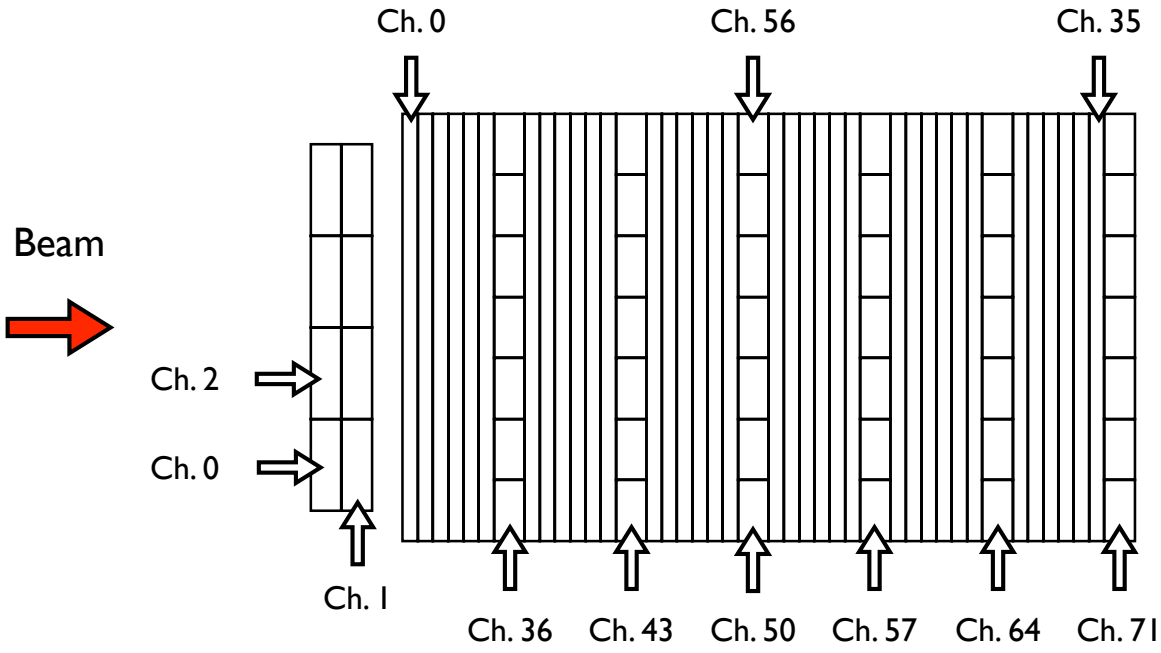

Figure 2.13: The Beam-Hole Charged Veto (BHCV, left) and Beam-Anti (BA, right). The scintillator layers of the BA are separated by vertical lines. The vertically stacked blocks are the quartz layers.

analysis. Therefore, the BA gain values were calibrated for each muon run. The values were extrapolated between runs by scaling with LED flasher data. The on-spill and off-spill corrections were obtained by making comparisons between on-spill and off-spill LED flasher signals.

The scintillator layers were calibrated using minimum ionizing energy deposits. GEANT3 estimated it to be 1.8 MeV/cm. The quartz layers were Cerenkov counters. We simulated the quartz channel light yield by using a "look-up table". The table was built from a study that computed the number of Cerenkov photons entering the PMTs as a function of energy and angle of charged particles passing through the quartz blocks. We chose to calibrate the quartz layers from data through counting of minimum ionizing particles (MIPs), and then scaled the MC using a muon run simulation to match that energy scale definition of photoelectrons to MIPs.

2.10.1 Beam-Hole Charged Veto

The Beam-Hole Charged Veto (BHCV) was made of eight scintillator plates, each 0.5 cm thick. The BHCV was designed to reject charged particles that travelled down the beam-pipe and somehow failed to trigger the BA veto. Because it sits forward of the BA, it helps to expand the solid area useful for vetoing.

2.11 The Vacuum System

The decay region was evacuated to 10^{-5} Pa. At 10^{-4} Pa, the background contribution for the E391a beam design is expected to be negligible (≤ 0.1 events) for a S.E.S. of $O(10^{-10})$ [16]. Because of the out-gassing from detector components, the decay region was separated from the detector components by a membrane. Regions outside the

membrane was kept at 0.1 Pa. Figure 2.14 shows the vacuum system.

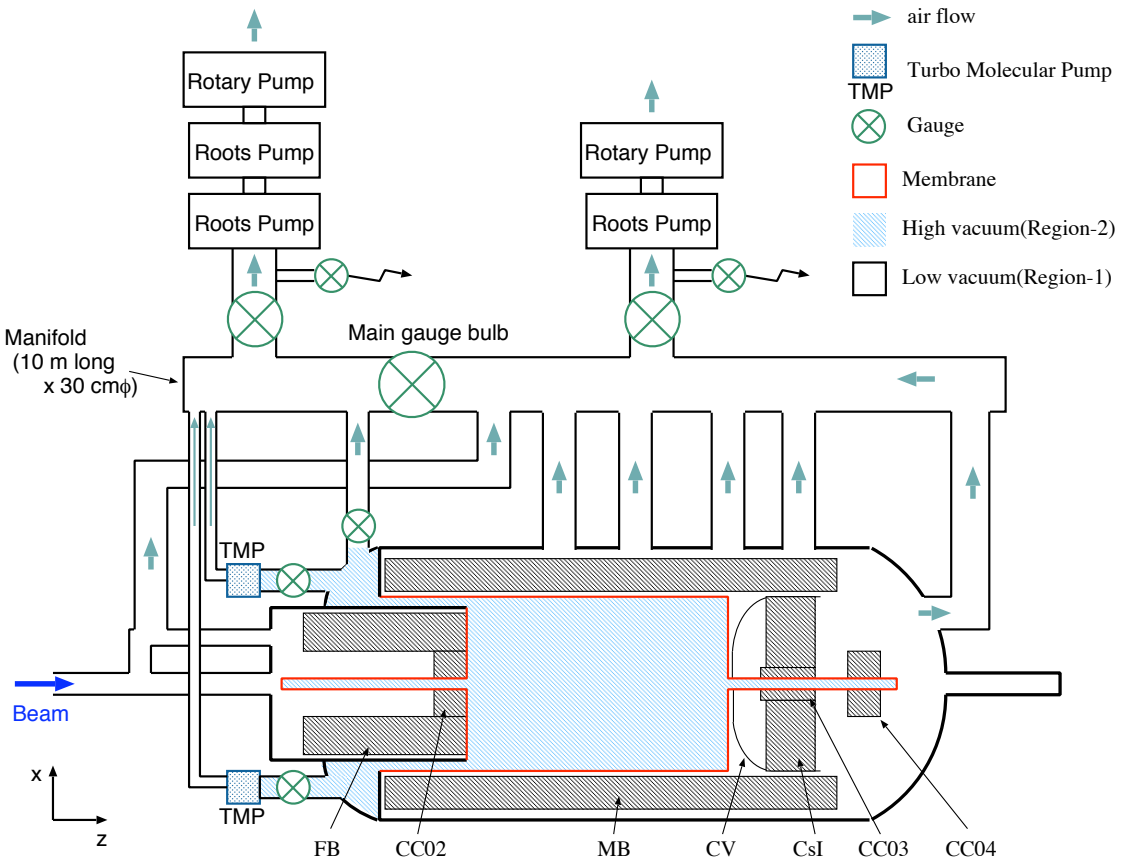

Figure 2.14: An iilustration of the vacuum system of E391a.

2.12 Calibration of CsI

Prior to installation, 25 KEK CsI crystals were tested with the KEK 3 GeV electron-hadron beam. Each crystal was also installed in a cosmic test bench and analyzed for response uniformity and to check the PMT attachments. The measured resolution is $\sim 1\% + 1\%/\sqrt{E}$.

After the CsI was installed, we performed three other forms of calibration. First, we

used cosmic rays to set an absolute energy scale. Second, we used $K_L^0 \to 3\pi^0$ decays and a constrained kinematic fit to refine the relative energy scale between crystals. Finally, we also used a special "Al-Target Run" to crosscheck both the absolute scale and relative scale between crystals. In the Al-Target Run, we inserted a 5 mm thick aluminum target in the beam directly in front of CC02. This target caused reactions like $n \to \pi^0 + X$ and gave a known vertex for $\pi^0 \to \gamma\gamma$ decays. We used a xenon flasher to monitor PMT gain drift and kept track of the temperature of the CsI and counter hall.

2.12.1 Cosmic Calibration

During Run II, a cosmic-ray trigger that took the coincidence of opposite modules of the Main Barrel was employed. We searched that sample of events for cases where we could identify a track in the CsI. Then we fit a path through the crystals in (x, y) space using a least-squares fit and rejected all tracks shorter than 70 cm in length or with poor χ^2 values. Figure 2.15 shows one such path. Deposited charge was normalized to path length through the crystal (with ambiguity in the path length on the z-axis being uncorrectable) and we assumed a minimum ionizing energy loss of 5.63 MeV/cm.

2.12.2 $K_L^0 \to 3\pi^0$ Calibration

We used a kinematic fit to constrain the relative energy between clusters in well-reconstructed $K_L^0 \to 3\pi^0$ decays [18]. Each photon cluster provides three measured variables, the (x, y) position and energy E along with their errors. There are three unknowns to solve for - the vertex of the kaon decay. There are six constraints:

- $M_{6\gamma} = M_{K_L}$ (K_L mass constraint)

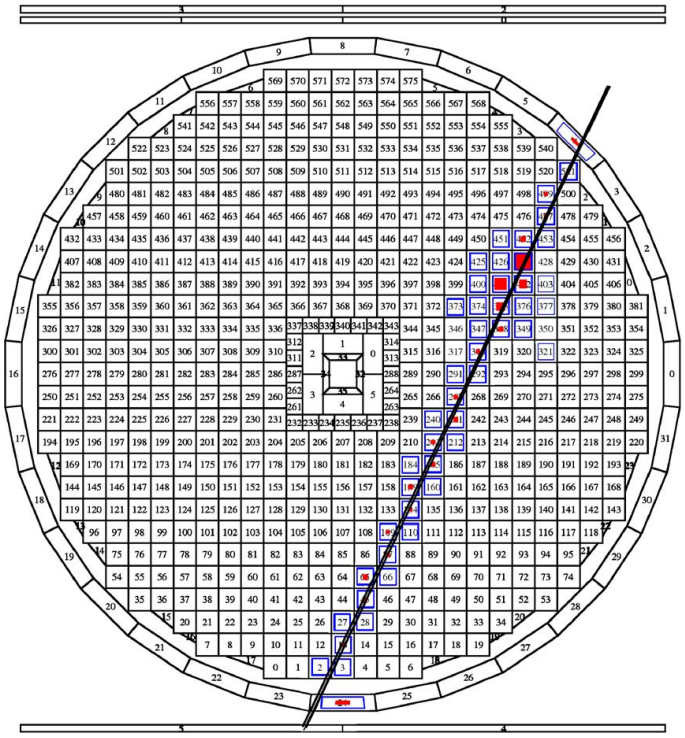

Figure 2.15: A cosmic ray track in the CsI calorimeter. The numbers indicate the crystal ID.

- $M_{\gamma\gamma} = M_{\pi^0}$ (π^0 mass constraint for three π^0)
- $\sum_i (x_i \times E_i) = v_x \times \sum_i E_i$ ("center of gravity" requirement)
- $\sum_i (y_i \times E_i) = v_y \times \sum_i E_i$ ("center of gravity" requirement)

This system can be solved by the method of Lagrange multipliers with three degrees of freedom. The energy and positions of the clusters are shifted to best satisfy the constraints.

To get the calibration factor, we can assume the energy of one cluster is unknown, increasing the number of unknown variables to four and leaving us with two degrees of freedom. The above method of Lagrange multipliers can be used to solve for the energy of that photon. The ratio between the measured and calculated energies can be used to shift the gain of the CsI crystals. This correction can be applied to all six photons. This procedure can be iterated to converge to stable calibration factors.

2.12.3 Al-Target Run

At the end of Run II, a 5 mm thick plate of aluminum was suspended 6.5 cm downstream from the end of CC02 for special Al-Target Runs. As mentioned before, Al-Target Runs can give a known vertex for $\pi^0 \to \gamma\gamma$ decays. In the usual event reconstruction, the π^0 mass is assumed. If there is a mistake in the overall energy scale, the reconstructed z-vertex will be shifted and such shifts will go undetected. In Al-Target Runs, we can use the known decay vertex to reconstruct π^0 without assuming a known mass. If there is a mistake in the overall energy scale, the reconstructed π^0 mass will also differ from the known value. We can update the calibration factors iteratively to correct such mistakes.

2.13 DAQ System Overview

The E391a experiment uses photo-multiplier tubes (PMTs) to convert scintillation light in detectors into electrical signals. The signals produced by the PMT's are sent to Amplifier-Discriminator modules which can take the input from the eight detector channels and produce individual analog signals for each channel together with an analog sum of the eight channels and a logic signal for a time-to-digital converter (TDC). The individual analog signals are sent to analog-to-digital converters (ADC's) by 90 m long coaxial delay cables. The sum signals are sent to the trigger logic for trigger decisons by 30 m coaxial cables. The logic signal for TDC is sent by a 30 m twisted pair cable with an additional 100 ns logic delay. The TDC's used a common start and individual stops. Figure 2.16 shows how the signals are sent from PMT's to TDC's.

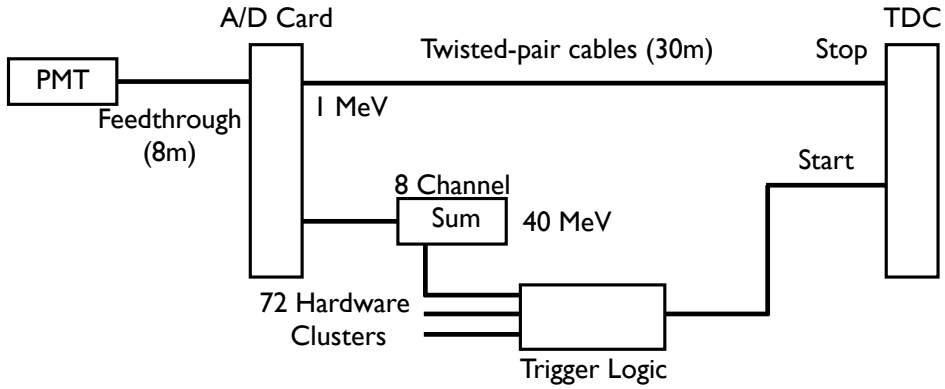

Figure 2.16: Signal transferred from PMT's to TDC's.

2.14 Triggering

2.14.1 Hardware Cluster

The CsI array is arranged into 72 different 8 block regions, forming the hardware clusters (HWC). Figure 2.17 shows the assignment of hardware clusters.

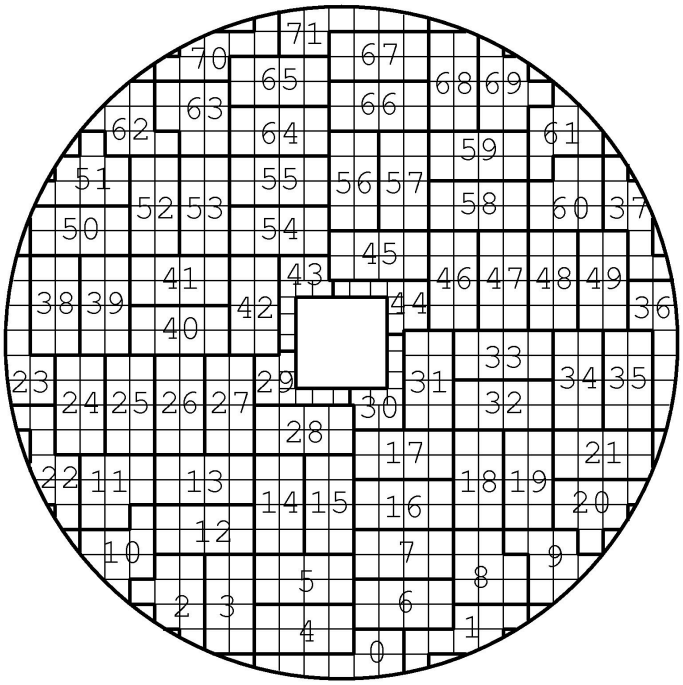

Figure 2.17: Layout of hardware clusters in the CsI array.

2.14.2 Online Vetoes

Loose vetoes (online vetoes) were applied during data taking to remove obvious backgrounds and to reduce the amount of data that needs to be stored. Table 2.14.2 displays the online veto thresholds used in Run II.

Detector	Electronics Threshold (mV)	Energy Equivalent (MeV)
CC02	-48.6	~ 25
CC03	-29	~ 15
CC04	-57.1	~ 45
CC05	-34.3	~ 25
Main Barrel (Upstream)	-31.2	~ 15
Front Barrel	-100	~ 30
Inner Charged Veto	-28.9	~ 1
Outer Charged Veto	-25.7	~ 1

Table 2.1: Representative parameters for the online veto thresholds in Run II (they were occasionally changed in response to ongoing analysis and electronics problems).

2.14.3 Physics Trigger

The physics trigger required that two or more HWC's passed the energy threshold of approximately 80 MeV per cluster and that no veto passed its threshold. This 80 MeV threshold was chosen to discriminate against soft beam secondaries and was comfortably below the ultimate analysis level cuts on minimum photon energy (at 150 MeV). This resulted in a trigger rate of roughly 200 Hz (roughly 400 triggers per 2 second beam spill).

2.14.4 Accidental Triggers

Three different accidental triggers were employed in E391a. The first was a trigger based on an energy sum threshold in BA. The second was based on an energy sum threshold in C6. The third was based on an energy threshold in a scintillator plane positioned adjacent to the target, the target monitor trigger. The target monitor trigger was proportional to beam intensity and was most effective in replicating data. Therefore, the target monitor trigger was used as the accidental trigger in later analysis.

2.14.5 Calibration Triggers and Minimum Bias Triggers

Several calibration triggers and a pair of minimum bias triggers were also used in E391a. The total trigger rate was approximately 500 Hz (1000 trigger requests per 2 second spill). For calibration we used a cosmic ray trigger based on energy deposition in opposing groups of channels in the main barrel. Additionally, we used a muon trigger based on the coincidence of CC02 and CC04.

The minimum bias triggers were designed to study the effects of the online vetoes by mimicking the cluster requirements of the physics trigger at interesting thresholds. One minimum bias trigger required only one or more HWC. The other required two or more HWC's.

2.15 Reconstruction

This section discusses how to reconstruct a kaon from the signals in our detectors.

2.15.1 Clustering

The first step in reconstruction is to find the photons that hit the CsI calorimeter. This process is done by the clustering algorithm as described below.

First, we find all possible cluster seeds (crystals with 5 MeV or more energy deposited). A list of all crystals with energy over 1 MeV is also compiled. Second, we try to grow the seed into potential clusters. We pick the seed crystal with the largest energy deposited and add crystals to the cluster by including neighbors (crystals that share an edge) from the list of cluster seeds. Crystals with more than 1 MeV energy deposition are also added to clusters where appropriate. We grow the cluster by adding qualified neighbors of neighbors until there is no qualified crystal to add. Then from

the list of remaining seed crystals we take the crystal with the highest energy and repeat the growing process. After all the seeds have been grown, we try to remove clusters that are likely to be fusion events. In each cluster, we count the number of local maxima (a local maximum is a crystal that has energy higher than all of its four neighbors). If any cluster has more than one local maximum, the event is rejected at this stage. In the end, usually there are crystals with energy below the seed threshold and seeds without neighbors. Such crystals are classified as single-hit crystals, which are not clusters. Many single-hit crystals are found on the diagonals of good clusters and are an artifact of the clustering algorithm. Some are due to soft photons. The width of most of the crystals is 7 cm and the Molliere radius in CsI is about 3.5 cm. Thus some electromagnetic showers are completely contained in single crystals. Finally, some single-hit crystals are due to other particles.

The "size" of a cluster is the number of crystals with energy deposition over 5 MeV. The "csize" of a cluster is the number of crystals with energy deposition over 1 MeV. These two sizes are used in the photon quality cuts.

The next step is to calculate the energy and position of the incident photon. Because the KEK crystals are 30 cm long, there is some leakage, which requires energy correction. The center-of-energy position also needs to be corrected. The correction tables were built from a Monte Carlo study, which injected photons into an 11×11 crystal array at different energies and angles. The correction is an iterative procedure. We first reconstruct a vertex using the reconstruction routine that will be described next. Using this vertex, we can go through the energy correction and the position and angle correction. With the corrected energy and position, we can reconstruct an updated vertex. This iterative procedure usually converges within three iterations.

2.15.2 Pion and Kaon Reconstruction

After we find photon clusters, we can reconstruct π^0's. Because we have a pencil beam, we assume the (x,y) position of π^0 is zero. The z position can be found by requiring the invariant mass of the two photons to be equal to the mass of π^0 :

$$\begin{aligned} m_\pi^2 &= (p_1 + p_2)^2 \\ &= p_1 p_1 + p_2 p_2 + 2 \times p_1 p_2 \\ &= 2 \times (E_1 E_2 - \mathbf{p_1} \cdot \mathbf{p_2}) \\ &= 2 E_1 E_2 \, (1 - \cos\theta) \end{aligned} \tag{2.1}$$

where p_i is the four momentum for the i-th photon (covariant notation is suppressed) and $\mathbf{p_i}$ is the three momentum for the i-th photon. Figure 2.18 illustrates the reconstruction.

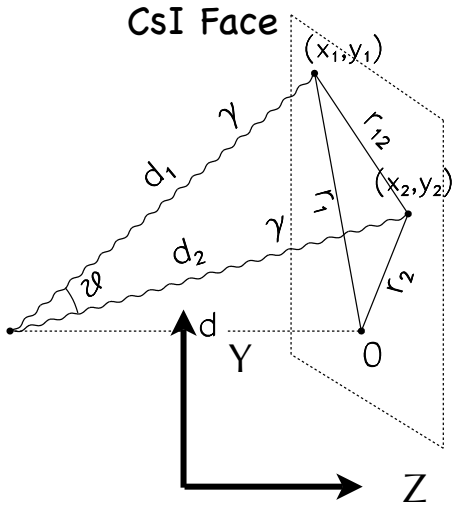

Figure 2.18: A diagramatic representation of π^0 reconstruction.

The next step is to reconstruct kaons from multiple π^0's. Different pairing of photons can lead to several possible combinations. The correct combination is selected

by the following pairing χ^2:

$$\chi^2 = \sum_{i=1}^{n} \frac{(z - \bar{z})^2}{\sigma_i^2}, \qquad \bar{z} = \frac{\sum_{i=1}^{n} z_i/\sigma_i^2}{\sum_{i=1}^{n} 1/\sigma_i^2}, \tag{2.2}$$

where n is the number of π^0 and σ is the result of error propagation on the uncertainty in the energy and position through Equation 2.1. Figure 2.19 illustrates this procedure for the case of $K_L^0 \to 3\pi^0$. The lowest-χ^2 combination is the preferred solution. In some cases the lowest χ^2 and the second lowest χ^2 are close and the correct combination could have a higher χ^2 because of fluctuation. Therefore, we not only require the lowest χ^2 to be small but also require the second lowest χ^2 to be large.

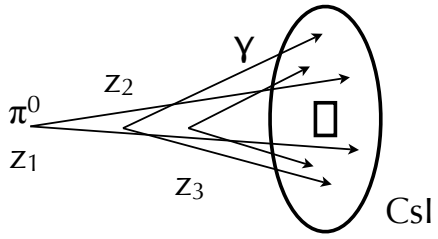

Figure 2.19: A diagramatic representation of $K_L^0 \to 3\pi^0$ reconstruction, where each pion is first reconstructed according to Figure 2.18.

CHAPTER 3

MONTE CARLO, EVENT SELECTION CRITERIA AND FLUX

3.1 Introduction

The consensus definition of kaon flux used in E391a is the number of kaons that decayed in the fiducial region which was chosen to be the region with z position between $300cm$ and $500cm$ for this analysis. $300cm$ was chosen to be downstream from CC02 and $500cm$ was chosen to be upstream from CsI calorimeter and CV. The kaon flux was calculated by two normalization modes $K_L^0 \to \pi^0\pi^0$ and $K_L^0 \to 3\pi^0$. The signal mode $K_L^0 \to \pi^0\pi^0\nu\bar{\nu}$ and the normalization mode $K_L^0 \to \pi^0\pi^0$ both have four photons in the final state and are more similar. So the flux calculated by $K_L^0 \to \pi^0\pi^0$ was used for later analysis.

The kaon Monte Carlo (MC) is used to calculate the acceptances of the normalization modes and the signal mode. Thus Monte Carlo simulation is a very important part of this analysis. The MC simulation was done using GEANT3. Kaons were generated at the end of the last collimator C6. They were not generated at the target in order to save CPU time. The generated kaons will be propagated and decay according to its life time and the decay mode specified. The decay products (except neutrinos) are tracked and propagated through each detector. The energy deposition and timing information of each channel of the detectors were stored in the same format as experimental data.

Raw MC will first go through the skimming routine, which applies loose veto cuts to simulate the online vetoes in data and also separates raw MC into different files based on the number of photon clusters identified. Then the skimmed MC will go through

reconstruction routines. Then they are ready to be analyzed.

3.1.1 Accidental Overlay

When protons hit the target, they can produce a large number of particles. Kaons are only a small fraction. Even after the absorbers and sweeping magnets, there are still other particles. When the beam enters our detector system, there are also photons and neutrons, which can cause false vetoes or false signals. Such accidental activities are not simulated in pure kaon MC. The solution is to use "Add-BG" Monte Carlo, which was an event-by-event overlay of MC and accidental data. Such Add-BG MC were used for later analysis.

3.2 Reweighted MC Events

Before the mass production of MC, the MC went through lots of tuning. But there was still some mismatch in the radial shape of the beam, which was because the kaon MC used a cylindially symmetric generator function while the real beam was ovular. Due to time constraint, mass production of MC started with this mismatch in the radial shape of the beam. In the end, we decided to reweight each MC event to match data. The radial distribution of kaon at C6 was the worst matching variable, so we decided to use the generated kaon radius at C6 to reweight MC events. The weight function is:

$$\begin{aligned} R^2_{Gen} &= \mathrm{gx}(1)^2 + \mathrm{gy}(1)^2, \\ W &= 1.305 - 0.192559 \times R^2_{Gen} + 0.0029822 \times \left(R^2_{Gen}\right)^2. \end{aligned} \tag{3.1}$$

where "gx" and "gy" are generated (x,y) position of kaon at C6. Figure 3.1 shows the Data/MC overlay of the reconstructed kaon radius at C6 with and without reweighting.

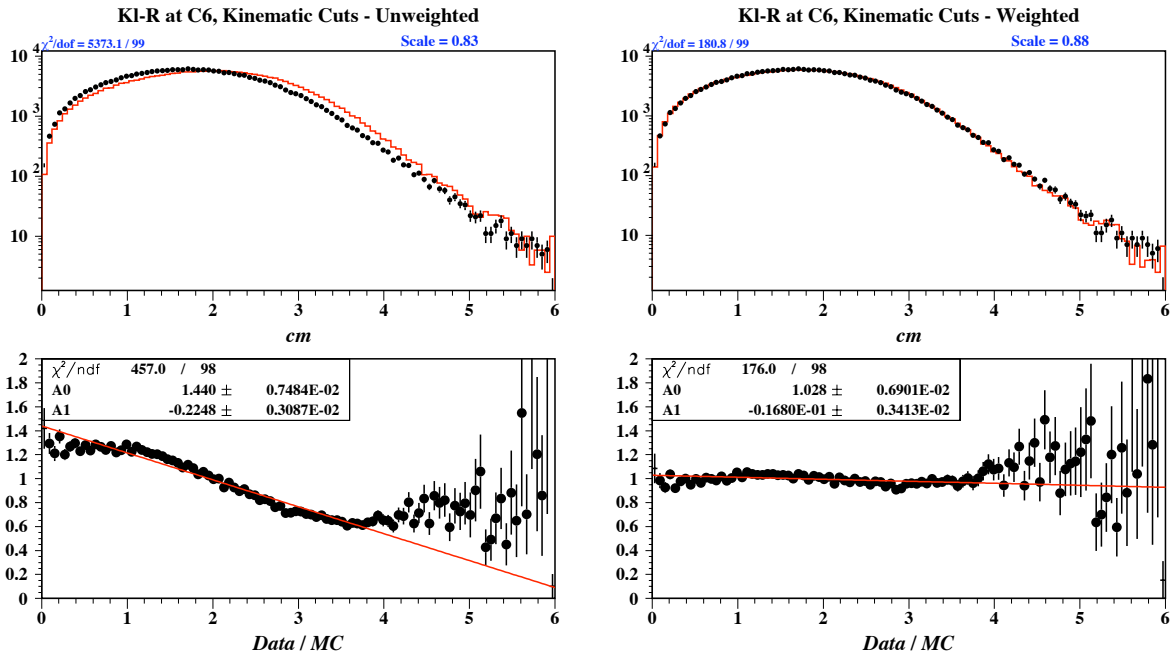

Figure 3.1: The reconstructed radius of the kaon at C6 before (left) and after (right) reweighting for six cluster ($K_L^0 \to 3\pi^0$) data and MC. All kinematic cuts (except the cut on kaon radius) are applied. In the upper half, data are shown as black dots with error bars and the MC events are shown in red. The lower half shows the bin-by-bin ratio of data and MC, normalized by total number of events. Here, the fit curve is $y = A_0 + A_1 \times r$. Errors on both data and MC are counting errors ($\sqrt{N}$). The $\chi^2/d.o.f.$ variable in the upper left-hand corner is a measure of bin-by-bin discrepancies. The scale variable in the upper right-hand corner is the number used to scale MC so that the total numbers of events for data and MC agree.

3.3 Event Selection

Event selection criteria are used to reject backgrounds and retain signal. There are two different kinds of event selection criteria, photon veto cuts and kinematic cuts. Photon

veto cuts almost correspond one to one to the photon veto detectors. Whenever energy deposition of a photon veto detector surpasses a certain threshold and the timing is within a certain timing window, the event will be cut out. Photon veto cuts usually only depend on one particle. Kinematic cuts usually depend on more than one particles and are usually based on the kinematic variables. Some kinematic cuts are used to select the correct pairing combination. Some kinematic cuts are photon quality cuts that are used to reject photon fusion events, hadronic showers or accidentals hits.

3.3.1 Photon Veto Cuts

Table 3.5 shows the photon veto cuts used in this analysis. The thresholds were chosen in two steps. In the first step, we chose the cut points to maximize the signal to noise ratio in the four cluster invariant mass distribution. The signal is the events in the kaon mass peak and the noise is the events in the sidebands. The following formula is a figure of merit:

$$S/N = \frac{(N_S/N_N)_{\text{After}}}{(N_S/N_N)_{\text{Before}}}. \tag{3.2}$$

In the second step, the vetoes were tightened to handle anticipated backgrounds.

The veto cuts also have timing windows. The time zero is the average time of the two highest energy photon clusters in the CsI. This time zero was subtracted from the time of each channel. The result is required to be within a certain timing window for the event to be rejected by the veto cut. The timing windows were chosen using two-cluster and four-cluster data. The timing distributions were fit by a Gaussian. MC cannot simulate timing information very well. For most detectors, the timing is simply the time of fight. So the timing windows of data and MC were different. The timing windows of data were chosen to be the intervals that were within a certain distance of

the mean, usually five or six sigma. The MC timing windows were chosen using the mean of MC timing distributions but with the same sigma as data.

The CsI calorimeter is used both for photon reconstruction and also as a very important veto. The clustering algorithm requires at least two crystals to form a cluster. The Moliere radius in CsI is about 3.5 cm and most of our crystals are $7cm \times 7cm$. It is pretty easy for a photon to deposit all of its energy in one crystal. Thus it is possible for a photon to hide itself in a single-hit crystal. Thus the CsI veto cut is a cut on such single-hit crystals. At the same time, the clustering algorithm does not grow the cluster in the diagonal directions. If we cut at very low energy thresholds, we will be sensitive to energy fluctuation. In the end, the energy threshold was chosen to be a function of the distance from the single-hit crystal to the nearest photon cluster. This choice also made CsI cut look both like photon veto cuts and kinematic cuts, which made it a very special cut.

3.3.2 Kinematic Cuts

Different decay modes have different kinematic variable distributions. So the kinematic cuts for different decay modes can also be different. Table 3.1 shows the kinematic cuts used for $K_L^0 \to 3\pi^0$. Table 3.2 shows the kinematic cuts used for $K_L^0 \to \pi^0\pi^0$.

Photon Energy Cut

The photon energy cut was employed to remove poorly reconstructed electromagnetic showers or low energy hadronic showers..

$3\pi^0$ Cut	Values	Comments
Photon Energy Min.	150 MeV	
Photon CsI Hit Position	$17.5 < r < 88$ cm	The inner dimension forms a square around the beam pipe, the outer is radial.
Photon Hit Separation Min.	17.5 cm	
Photon Fusion Neural Network Min.	0.5	
Pion z-difference Max.	10 cm	
Pion Mass-difference Max.	5.125 MeV/c^2	
Best z-χ^2 Max.	3	
2nd Best Minus Best z-χ^2 Min.	4	
r^2 at C6 Max.	4.5 cm^2	Also cut if $r(z_{decay})$ is less than R(C6).
Decay z	$300 < z < 500$ cm	
Transverse Momentum Max.	1.25×10^{-4} (GeV/c)^2	

Table 3.1: Kinematic Cuts for Six-Cluster Events.

Photon Fiducial Cut

This cut is a cut on the photon hit (x,y) position on CsI. The inner square surrounding the KTeV crystals is excluded. To guarantee the quality of reconstructed photon clusters, the edge of the CsI calorimeter is also excluded.

Gamma RMS

The RMS for a photon cluster is computed according to the following formula:

$$RMS = \sqrt{\frac{\sum_{crystals} E_i \times (\mathbf{r_i} - \mathbf{r_0})^{\mathbf{2}}}{\sum_{crystals} E_i}}, \tag{3.3}$$

Cut	Values	Comments
Photon Energy Min.	150 MeV	
Photon CsI Hit Position	$17.5 < r < 88$ cm	The inner dimension forms a square around the beam pipe, the outer is radial.
Photon Hit Separation Min.	19 cm	
Photon Fusion Neural Network Min.	0.8	
Pion z-difference Max.	5.5 cm	
Pion Mass-difference Max.	3 MeV/c^2	
Best χ^2 Max.	3	
2nd Best minus Best χ^2 Min.	4.5	
r^2 at C6 Max.	5.5 cm^2	Also cut if $r(z_{decay})$ is less than R(C6).
Decay z	300 <z< 500 cm	
Transverse Momentum Max.	1.25×10^{-4} (GeV/c)^2	

Table 3.2: Kinematic Cuts for Four-Cluster Events.

where $\mathbf{r_0}$ is the vector from the origin of the CsI face to the center of the cluster and $\mathbf{r_i}$ is the vector from the origin to the center of the i^{th} crystal in the cluster. It measures the energy weighted mean radial dispersion of a cluster. It is sensitive to fusion events, but also sensitive to clusters formed by very high angles of incidence.

TDI

TDI is a measure of time dispersion in a cluster and is defined by the following formula:

$$TDI = \frac{\sqrt{\sum_{crystals}(T_i - T_{mean})^2}}{N_{crystals}}, \tag{3.4}$$

where T_{mean} is the average time for all the crystals with energy deposition above the TDC threshold of ~ 1 MeV. The TDI cut is like a time fusion cut. The TDI distribution

cannot be replicated in MC, so we estimated the acceptance loss by using $K_L^0 \to \pi^0\pi^0$ signal events in data.

Gamma Energy Ratio

The Gamma energy ratio is defined as

$$\frac{E_1 + E_2 + E_3}{\sum E_i}. \tag{3.5}$$

where E_1, E_2 and E_3 are the energy depositions of the three highest energy crystals and E_i are the energies in the individual crystals. It serves as a fusion cut and it can also remove hadronic showers and poorly reconstructed electromagnetic showers.

Fusion Neural Network

The neural network was used to classify photon clusters into fusion and nonfusion clusters. It has 12 inputs, 10 hidden nodes and 1 output. The inputs are the energy deposition in the nine blocks surrounding the center of the photon cluster normalized by the total energy, the (x,y) position of the cluster and the azimuthal angle. Figure 3.2 illustrates the neural network.

The weighted sums of the inputs transformed by the sigmoid function give the hidden nodes, which are used to give the output.

$$y_j = \sigma(\sum_{k=1}^{n} W_{jk}x_k + B_j), z_i = \sigma(\sum_{j=1}^{m} W_{ij}x_j). \tag{3.6}$$

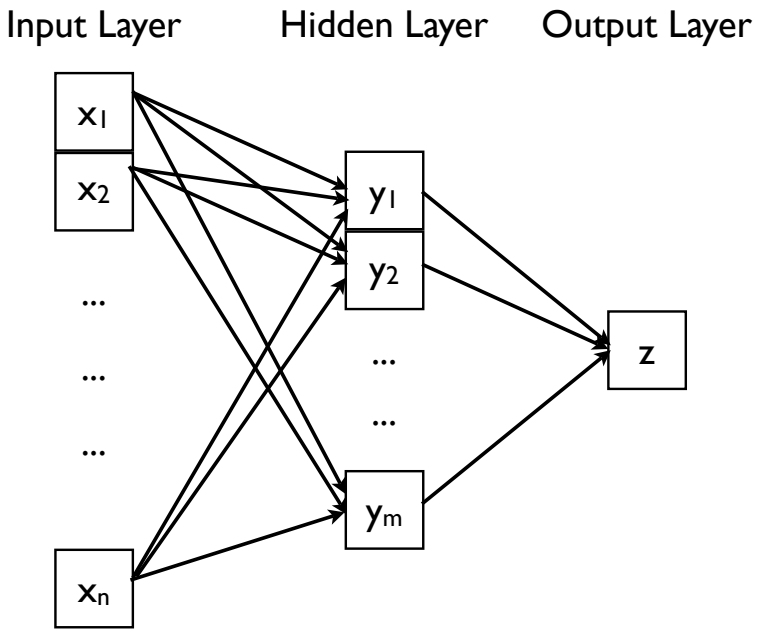

Figure 3.2: Illustration of the neural network.

where σ is a sigmoid function:

$$\sigma(x) = \frac{1}{1+e^{-x}}. \tag{3.7}$$

The training samples for fusion clusters were taken from $K_L^0 \to 3\pi^0$ MC with five clusters identified and six clusters striking CsI. The training samples for nonfusion clusters were taken from well reconstructed $K_L^0 \to 3\pi^0$ events in data.

Pairing χ^2

This was already discussed in kaon reconstruction.

3.4 Data/MC Comparison

The acceptances of the normalization modes and the signal modes are computed from MC. Thus, it is very important that MC and data can match well. This section will examine this issue by comparing data and MC for several important kinematic variables.

3.4.1 Convention and Normalization

Reweighting function, Equation 3.1, was applied in the following Add-BG MC. Several Data/MC overlay plots will be shown. The usual conventions for such overlay plots are that data are represented by black dots and MC are represented by red curves. The lower halves of such plots plot the ratio of Data/MC.

Relative normalization was used in the following plots because there was still some discrepancy between the flux estimates from $K_L^0 \to \pi^0\pi^0$ and $K_L^0 \to 3\pi^0$. So data and MC were normalized either by total events or by signal events which are events with invariant mass between 481.4 MeV and 512.6 MeV. This range was obtained from the 3σ mass window in the $3\pi^0$ invariant mass distribution.

3.4.2 Overlay Plots

The first variable we will compare is the decay z vertex of kaons. Figure 3.3 shows the decay z vertex distribution for four-cluster events. Figure 3.4 shows the decay z vertex distribution for six-cluster events.

Figure 3.5 and Figure 3.6 show the total momentum distributions for four-cluster events and six-cluster events. The discrepancy was mainly because the CsI cut was not simulated very well as explained in [19].

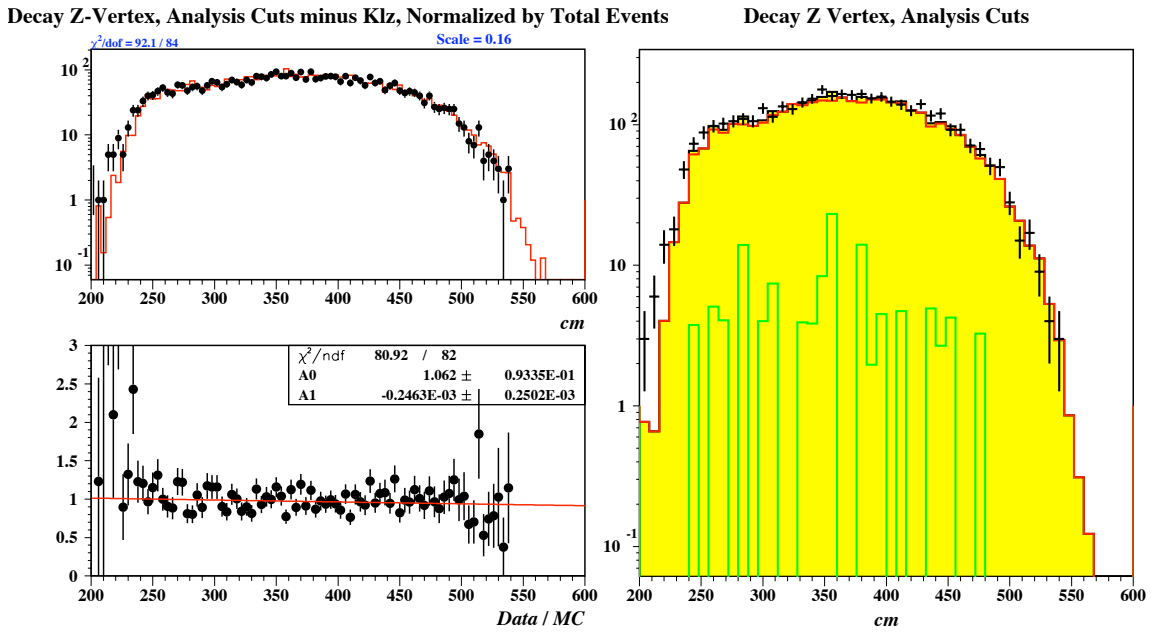

Figure 3.3: The four-cluster decay z distribution normalized by total events. All analysis cuts are applied except the cut on the z vertex. In the figure on the right, green line represents $\pi^0\pi^0\pi^0$ MC, red line represents $\pi^0\pi^0$ MC and solid yellow represents the sum of those MC. Data is represented by black dots with error bars.

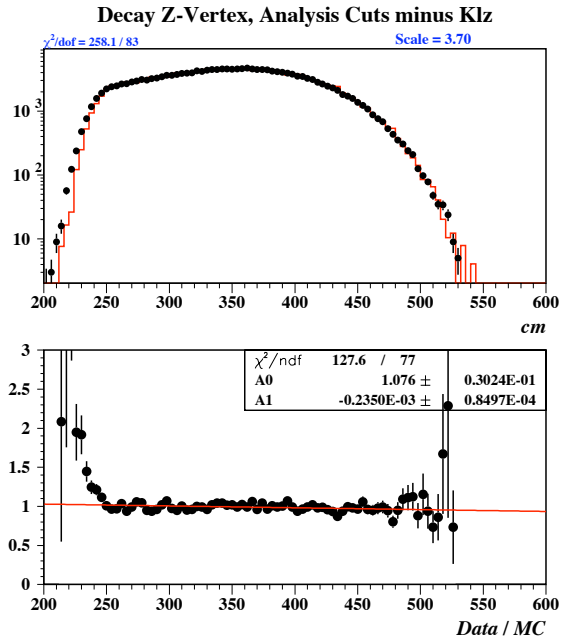

Figure 3.4: The six-cluster decay z distribution normalized by total events. All analysis cuts are applied except the cut on the z vertex.

The transverse momentum distributions (P_T) of kaons for four-cluster and six-cluster events are shown in Figure 3.7 and 3.8. The transverse momentum is defined relative to the nominal beam axis. The actual beam direction in Run II was pointing slightly down and to the left relative to the nominal z axis. But the error introduced in P_T is negligible.

Another variable that is closely related to the P_T distribution is the kaon radius at C6, where the kaons are generated. Figure 3.9 and Figure 3.10 show the distribution of kaon radius at C6 for four-cluster and six-cluster events.

The most important variable is the invariant mass of the photon clusters identified in CsI. Figure 3.11 shows the six-cluster invariant mass distribution. Figure 3.12 shows the four-cluster invariant mass distribution. They are normalized by signal events as defined at the beginning of this section. In the four-cluster invariant mass distribution,

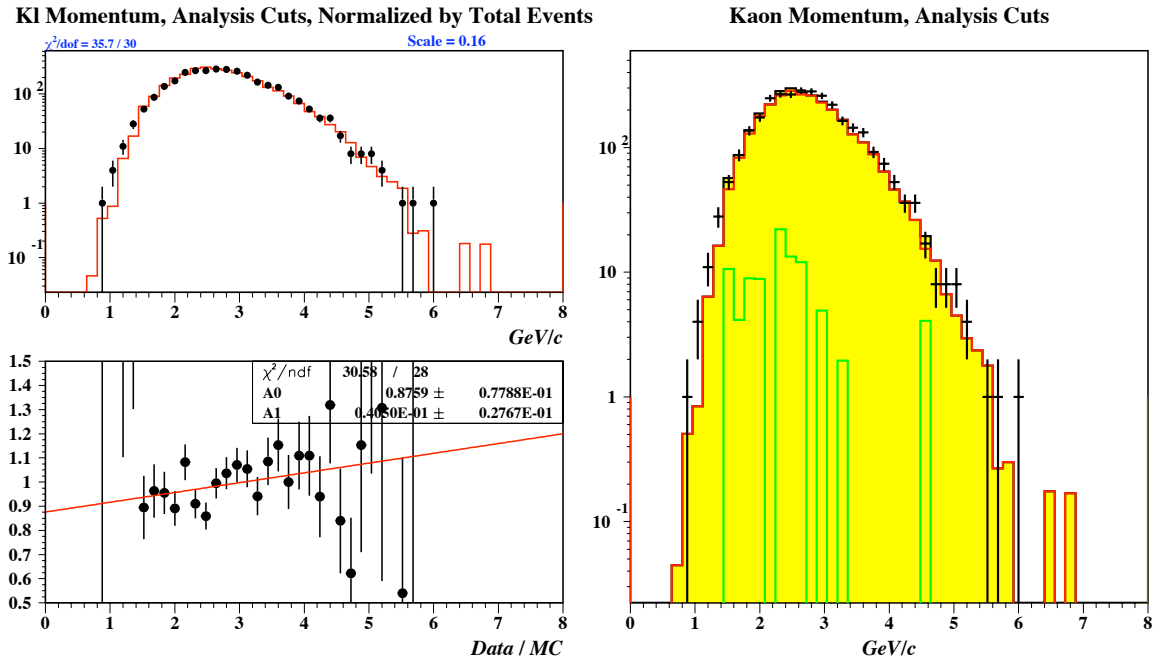

Figure 3.5: The kaon total momentum distribution for four-cluster events. All analysis cuts are applied. In the figure on the right, green line represents $\pi^0\pi^0\pi^0$ MC, red line represents $\pi^0\pi^0$ MC and solid yellow represents the sum of those MC. Data is represented by black dots with error bars.

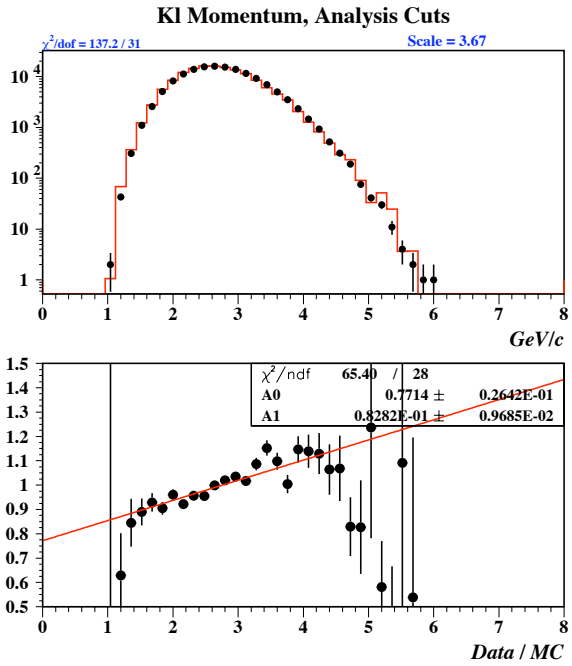

Figure 3.6: The kaon total momentum distribution for six-cluster events. All analysis cuts are applied.

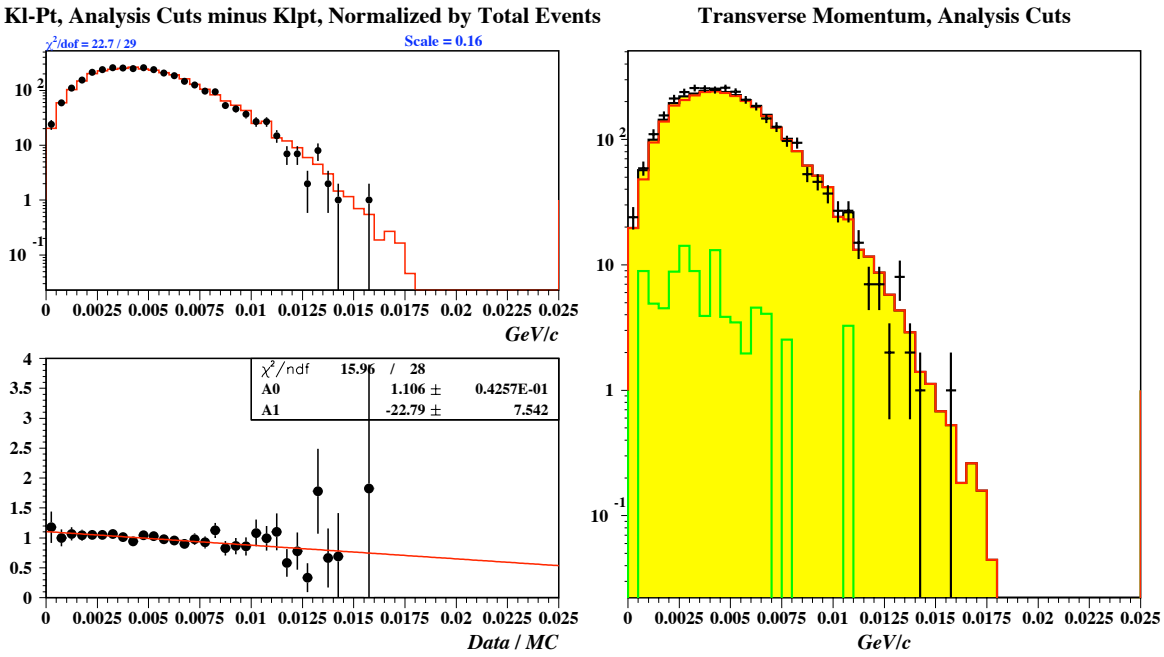

Figure 3.7: The kaon transverse momentum distribution for four-cluster events. All analysis cuts are applied except for the cut on transverse momentum. In the figure on the right, green line represents $\pi^0\pi^0\pi^0$ MC, red line represents $\pi^0\pi^0$ MC and solid yellow represents the sum of those MC. Data is represented by black dots with error bars.

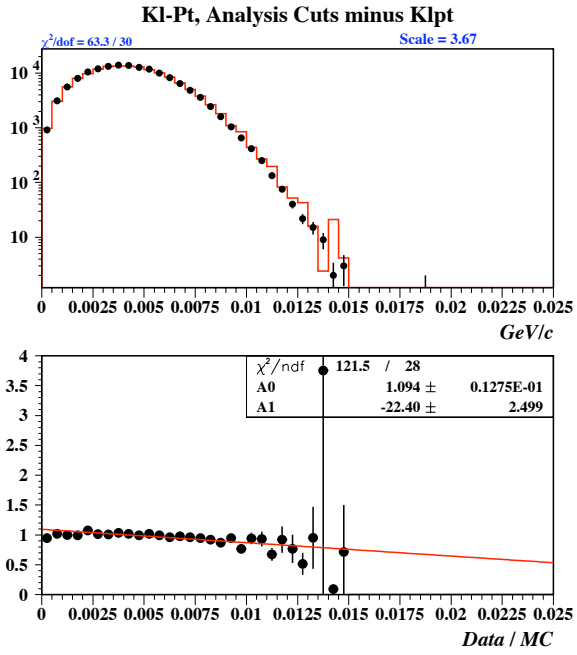

Figure 3.8: The kaon transverse momentum distribution for six-cluster events. All analysis cuts are applied except for the cut on transverse momentum.

the events below the mass peak are usually due to $K_L^0 \to 3\pi^0$ with two missing photons or one missing photon and one photon fusion cluster or two photon fusion clusters. The events above the mass peak are usually due to false combinatorics. There are eleven events above the mass peak in data. There is almost zero event in MC. Our $\pi^0\pi^0\pi^0$ MC is only about 25% of data. This discrepancy could be due to statistical fluctuation. The imperfect simulation of CsI can also be a reason.

3.5 Flux and Systematic Error

This section will give the kaon flux of Run II and the systematic error of the flux.

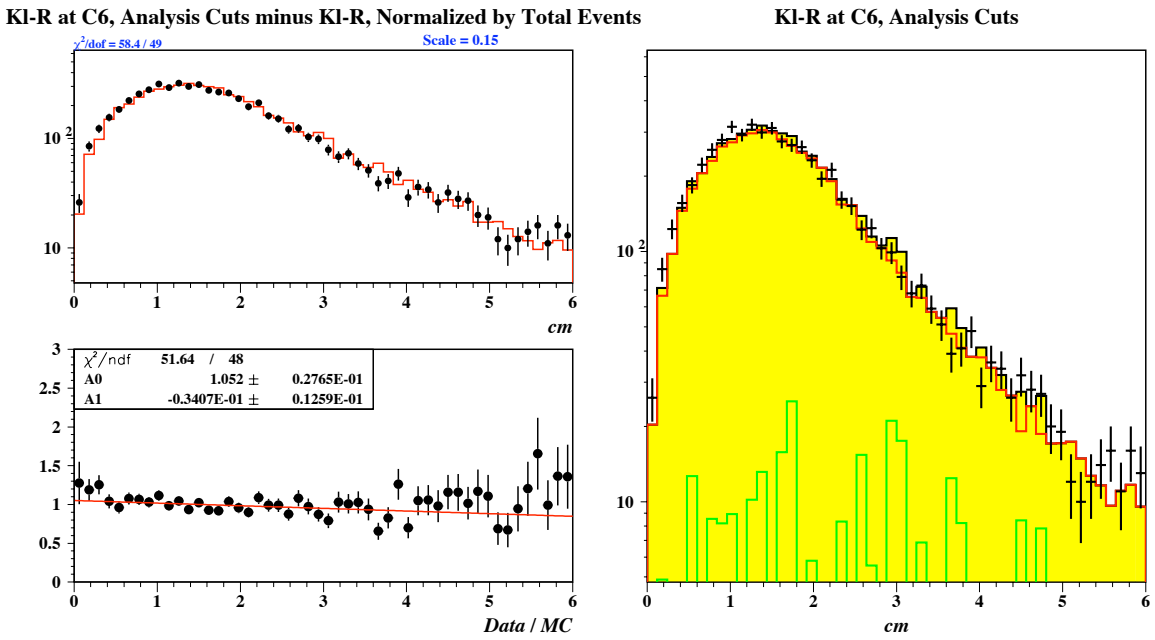

Figure 3.9: The distribution of kaon radius at C6 for four-cluster events. All analysis cuts are applied except for the cut on kaon radius. In the figure on the right, green line represents $\pi^0\pi^0\pi^0$ MC, red line represents $\pi^0\pi^0$ MC and solid yellow represents the sum of those MC. Data is represented by black dots with error bars.

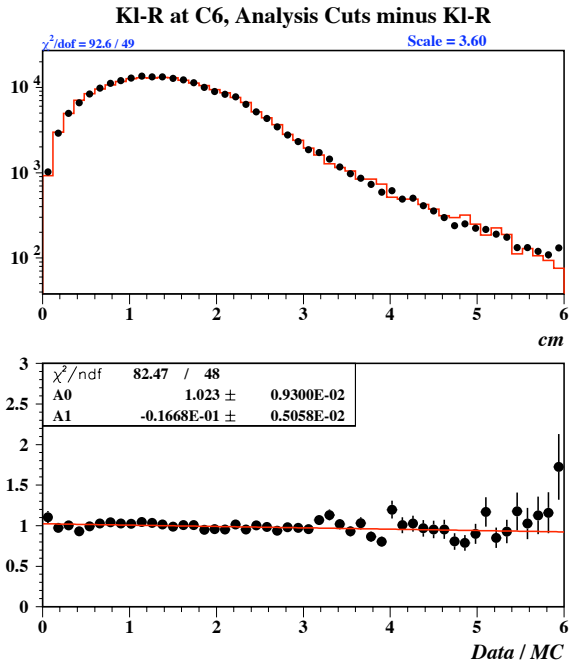

Figure 3.10: The distribution of kaon radius at C6 for six-cluster events. All analysis cuts are applied except for the cut on kaon radius.

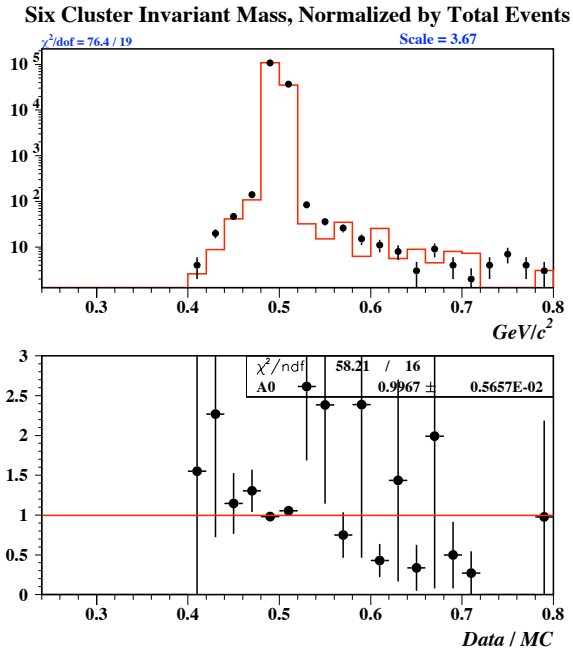

Figure 3.11: The distribution of six-cluster invariant mass. All analysis cuts are applied except for the cut on kaon radius.

3.5.1 Flux

As mentioned at the beginning of this chapter, the kaon flux is the number of kaons that decayed in the fiducial region which was the region with z position between $300cm$ and $500cm$. The flux is calculated following the following formula:

$$\text{Flux} = \frac{\text{N}_{\text{Signal}}}{\text{Acceptance} \times \text{Branching Ratio}} \tag{3.8}$$

where the acceptance is defined as:

$$\text{A} = \frac{N_{Obs}}{N_{decay}} = \frac{N_{Obs}}{N_{C6} \times p_d}, \tag{3.9}$$

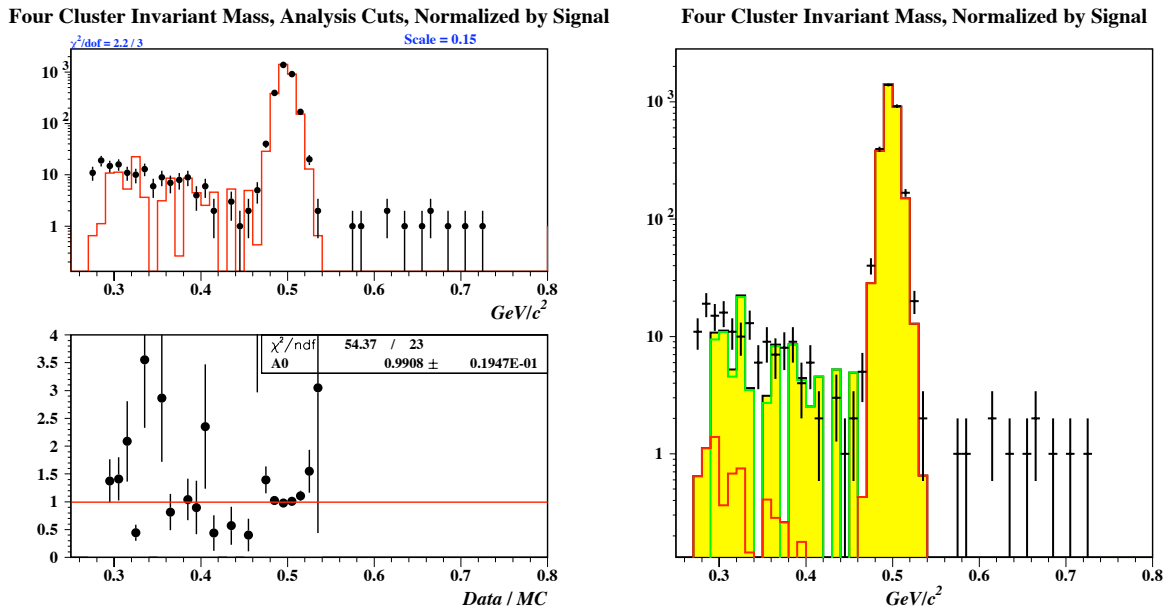

Figure 3.12: The distribution of four-cluster invariant mass. All analysis cuts are applied except for the cut on kaon radius. In the figure on the right, green line represents $\pi^0\pi^0\pi^0$ MC, red line represents $\pi^0\pi^0$ MC and solid yellow represents the sum of those MC. Data is represented by black dots with error bars.

where N_{C6} is the number of Kaons at C6 and p_d is the probability of kaons decaying in the fiducial region.

The decay probability was calculated by a special Monte Carlo, where the interactions with all the detectors were turned off. In this special MC, the number of kaons that decayed in the fiducial region divided by the number of kaons generated at C6 will give the decay probability. The decay probability is given in Table 3.3.

Events Generated at C6 - Raw	500,000
Decays in the Fiducial [300,500] - Weighted	13,414.8
Weighted Decay Probability	$(2.68 \pm 0.0232_{Stat}) \times 10^{-2}$

Table 3.3: Decay probability.

The acceptances and flux estimates by the two normalization modes, $K_L^0 \to \pi^0\pi^0$ and $K_L^0 \to 3\pi^0$, are given in Table 3.4.

Mode	Acceptance	Flux
$K \to \pi^0\pi^0$	$(3.05 \pm 0.03) \times 10^{-4}$	$(5.61 \pm 0.16) \times 10^9$
$K \to \pi^0\pi^0\pi^0$	$(1.36 \pm 0.01) \times 10^{-4}$	$(5.43 \pm 0.03) \times 10^9$

Table 3.4: Acceptance and flux estimates. Errors are only statistical.

3.5.2 Systematic Error and Flux Value

As hinted before, the MC simulation cannot perfectly replicate data. Thus there can be systematic error in the flux estimate. The systematic error is obtained using the following formula:

$$\text{Syst. Err.}^2 = \frac{\sum_{i=\text{All Cuts}} \left(F_i/A_{Data,i}\right)^2}{\sum_{i=\text{All Cuts}} \left(1.0/A_{Data,i}\right)^2}, \tag{3.10}$$

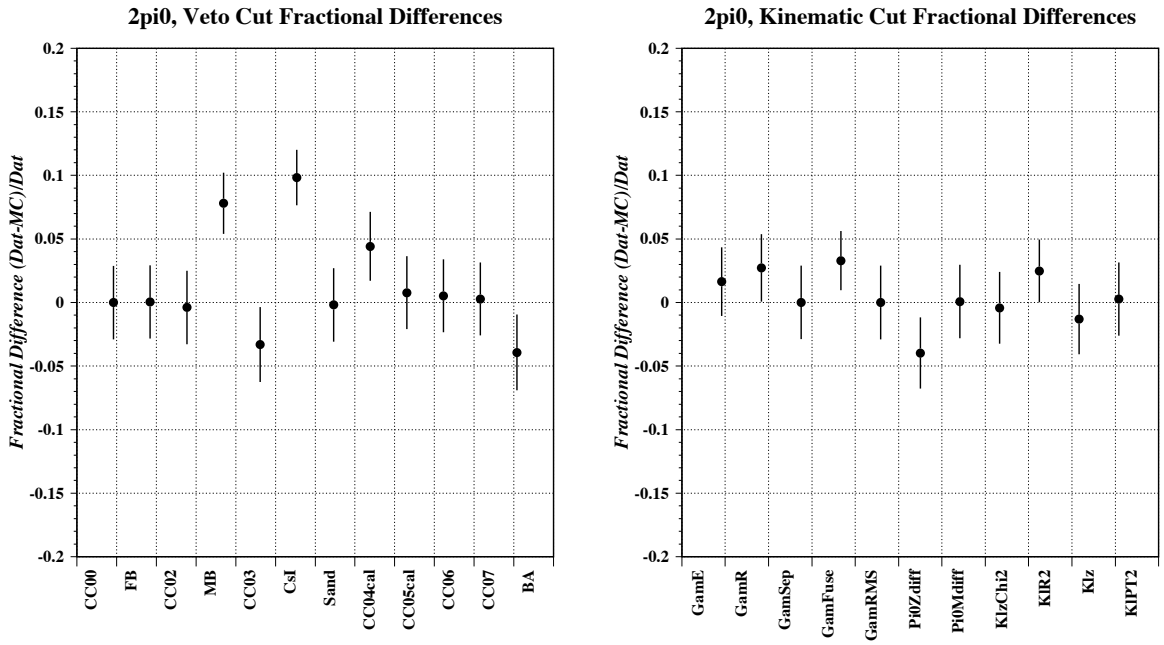

Figure 3.13: The figure on the left shows the fractional differences for photon veto cuts. The figure on the right shows the fractional differences for the kinematic cuts used for $K_L^0 \to \pi^0\pi^0$.

where A, the exclusive acceptance, is defined as the acceptance of a given cut with all other cuts applied. F, the fractional difference, is the exclusive acceptance of data minus the exclusive acceptance of the MC, divided by the exclusive acceptance of data. The acceptance weighted fractional difference, F/A, is the fractional difference divided by the exclusive acceptance of data. The weights were chosen to give more weights to more important cuts (cuts with lower exclusive acceptances).

Figure 3.13 shows the fractional differences for $K_L^0 \to \pi^0\pi^0$. The CsI cut has the largest fractional difference because CsI veto is sensitive to energy scale errors. Because we cannot use a drift chamber to measure the energy resolution precisely, it is likely to have an energy scale error. The systematic error calculated using Equation 3.10 is 4.7%. The flux given by $K_L^0 \to \pi^0\pi^0$ is chosen because it has more similarity with the signal mode $K_L^0 \to \pi^0\pi^0\nu\bar{\nu}$. Therefore, the flux value with systematic error is $(5.61 \pm 0.31) \times 10^9$.

Detector	Energy Cut	Comments
CC00	2 MeV	
Front Barrel	1 MeV	Inner & Outer Sum.
CC02	1 MeV	
Barrel CV	0.75 MeV	$\sqrt{Up \times Down}$ (w/TDC).
Inner Main Barrel	1 MeV	$\sqrt{Up \times Down}$ (w/TDC).
Outer Main Barrel	1 MeV	$\sqrt{Up \times Down}$ (w/TDC).
Outer CV	0.3 MeV	
Inner CV	0.7 MeV	
CC03	2 MeV	
CsI: S-Hit Close	10 MeV	Crystal $d < 20$ cm from closest cluster.
CsI: S-Hit Intermediate	5 - $(1/10)(d - 20)$ MeV	Crystal is d cm from closest cluster.
CsI: S-Hit Far	1.5 MeV	Crystal $d > 50$ cm from closest cluster.
Sandwich Counters	2 MeV	
CC04 Charged Layer	0.7 MeV	
CC04 Calorimeter Layer	2 MeV	
CC05 Charged Layer	0.7 MeV	
CC05 Calorimeter Layer	3 MeV	
CC06	10 MeV	Cerenkov detector with MIP calibration
CC07	10 MeV	Cerenkov detector with MIP calibration
BHCV	0.1 MeV	
BA Scintillator BA Quartz	20 MeV 0.5 MIPs	Sum over layers. Max. layer. (AND logic.)

Table 3.5: The photon veto cuts.

CHAPTER 4

BIFURCATION METHOD AND BACKGROUND ESTIMATION

4.1 Motivation

For this analysis, the most important part is the background estimation. The usual way of background estimation is to use MC simulation. For the signal mode $K_L^0 \to \pi^0\pi^0\nu\bar{\nu}$, the dominant background source is due to $K_L^0 \to 3\pi^0$ with two missing photons, one missing photon and one photon fusion or two photon fusions. Because we chose to simulate the full electromagnetic shower and the branching ratio of $K_L^0 \to 3\pi^0$ is pretty high (almost 20%), it takes a lot of CPU time to simulate even 25% of data. So we turned to another method, bifurcation, to do background estimation, which predicts background using data without opening the signal box.

This chapter will first introduce the bifurcation method with fairly detailed derivation. Full details about the derivation can be found in [21]. Then the background estimation will be given following the bifurcation method.

4.2 Bifurcation Method

This method was first developed in experiments E787 and E949 at Brookhaven [20]. I will first introduce the method for one background source and independent cuts. Then the it will be extended to deal with multiple background sources or weakly correlated cuts.

4.2.1 One background Source

Here the setup cuts have already been applied to eliminate all other background sources. The goal is to estimate the number of background events in the signal box that pass all the cuts. Besides setup cuts, there are also cuts A and B. Let N_0 denote the number of background events that pass the setup cuts and $P(AB)$ is the cut survival probability (CSP), probability for the background source to pass cuts A and B. Then the number of background events is

$$N_{bkg} = N_0 P(AB). \tag{4.1}$$

If cuts A and B are independent, then we have

$$P(AB) = P(A)P(B) \tag{4.2}$$

$$N_{bkg} = N_0 P(A)P(B) \tag{4.3}$$

which can be rewritten as

$$N_{bkg} = \frac{N_0^2 P(A)P(B)P(\bar{A})P(\bar{B})}{N_0 P(\bar{A})P(\bar{B})} \tag{4.4}$$

where $\bar{A}$ and $\bar{B}$ are the inverses of cuts A and B. If we define the following quantities:

$$N_{A\bar{B}} = N_0 P(A)P(\bar{B}) \tag{4.5}$$

$$N_{\bar{A}B} = N_0 P(\bar{A})P(B) \tag{4.6}$$

$$N_{\bar{A}\bar{B}} = N_0 P(\bar{A})P(\bar{B}) \tag{4.7}$$

then Equation 4.4 can be written as

$$N_{bkg} = \frac{N_{A\bar{B}} N_{\bar{A}B}}{N_{\bar{A}\bar{B}}} \tag{4.8}$$

Since $N_{A\bar{B}}$, $N_{\bar{A}B}$ and $N_{\bar{A}\bar{B}}$ are outside the multidimensional signal box defined by setup cuts and cuts A and B, Equation 4.8 allows us to predict backgrounds without opening the signal box. Figure 4.1 illustrates the distribution of background events in the cut space.

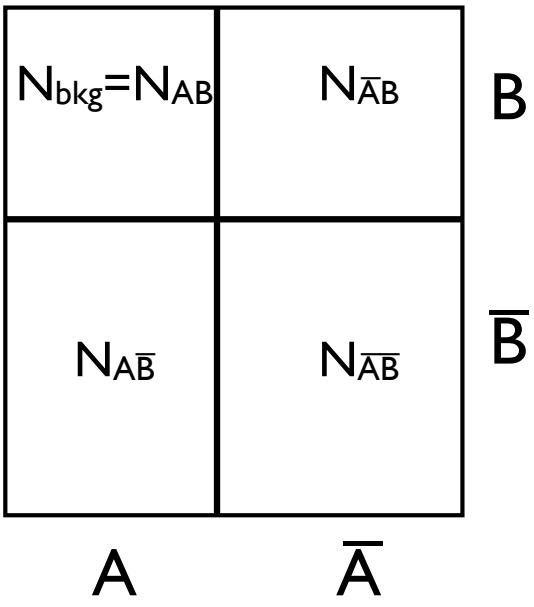

Figure 4.1: Illustration of the background events distribution in the cut space.

4.2.2 Multiple Background Sources

When there are multiple background sources after setup cuts are applied, the background prediction is not as simple as the single background source case. I will use the

case of two background sources as an example. The result can be extended to three or more background sources.

Suppose the backgound is made up of two sources $N_0 = N_1 + N_2$. We can still define similar quantities:

$$N_{bkg} = N_1 P_1(A) P_1(B) + N_2 P_2(A) P_2(B) \tag{4.9}$$

$$N_{A\bar{B}} = N_1 P_1(A) P_1(\bar{B}) + N_2 P_2(A) P_2(\bar{B}) \tag{4.10}$$

$$N_{\bar{A}B} = N_1 P_1(\bar{A}) P_1(B) + N_2 P_2(\bar{A}) P_2(B) \tag{4.11}$$

$$N_{\bar{A}\bar{B}} = N_1 P_1(\bar{A}) P_1(\bar{B}) + N_2 P_2(\bar{A}) P_2(\bar{B}) \tag{4.12}$$

If we plug the above definitions into the right-hand side of Equation 4.8, we have

$$\frac{N_{A\bar{B}} N_{\bar{A}B}}{N_{\bar{A}\bar{B}}} = \frac{[N_1 P_1(A) P_1(\bar{B}) + N_2 P_2(A) P_2(\bar{B})][N_1 P_1(\bar{A}) P_1(B) + N_2 P_2(\bar{A}) P_2(B)]}{N_{\bar{A}\bar{B}}} \tag{4.13}$$

The numerator can be expanded into the following:

$$\begin{aligned} N_{A\bar{B}} N_{\bar{A}B} = {} & N_1^2 P_1(A) P_1(\bar{A}) P_1(B) P_1(\bar{B}) + N_2^2 P_2(A) P_2(\bar{A}) P_2(B) P_2(\bar{B}) \\ & + N_1 N_2 [P_1(A) P_2(\bar{A}) P_2(B) P_1(\bar{B}) + P_2(A) P_1(\bar{A}) P_1(B) P_2(\bar{B})]. \end{aligned} \tag{4.14}$$

On the other hand, if we multiply N_{bkg} with the denominator, we have

$$\begin{aligned} N_{bkg} N_{\bar{A}\bar{B}} = {} & N_1^2 P_1(A) P_1(\bar{A}) P_1(B) P_1(\bar{B}) + N_2^2 P_2(A) P_2(\bar{A}) P_2(B) P_2(\bar{B}) \\ & + N_1 N_2 [P_1(A) P_2(\bar{A}) P_1(B) P_2(\bar{B}) + P_2(A) P_1(\bar{A}) P_2(B) P_1(\bar{B})] \end{aligned} \tag{4.15}$$

Comparing Equation 4.14 and 4.15 and using relations like $P_i(\bar{A}) = 1 - P_i(A)$, we have

$$N_{bkg} = \frac{N_{A\bar{B}} N_{\bar{A}B}}{N_{\bar{A}\bar{B}}} + \frac{N_1 N_2}{N_{\bar{A}\bar{B}}} \Delta(A)\Delta(B). \tag{4.16}$$

where $\Delta(A) = P_2(A) - P_1(A)$ and $\Delta(B) = P_2(B) - P_1(B)$. Compared with the single backgound source case, there is a correction due to the different CSP's of the two background sources. The above derivation can be extended to n background sources:

$$N_{bkg} = \frac{N_{A\bar{B}} N_{\bar{A}B}}{N_{\bar{A}\bar{B}}} + \sum_{1 \le i < j \le n} \frac{N_i N_j}{N_{\bar{A}\bar{B}}} \Delta_{i,j}(A)\Delta_{i,j}(B). \tag{4.17}$$

where $\Delta_{i,j}(A) = P_i(A) - P_j(A)$ and $\Delta_{i,j}(B) = P_i(B) - P_j(B)$.

4.2.3 Cuts with Correlation

When cuts A and B are not independent, the correlation between cuts A and B will have an impact on the background estimation. A correction when there is weak correlation between cuts A and B will be given. When there is correlation between A and B, the relevant quantities have to be expressed in terms of conditional probabilities:

$$N_{bkg} = N_0 P(AB) = N_0 P(A|B)P(B), \tag{4.18}$$

$$N_{A\bar{B}} = N_0 P(A\bar{B}) = N_0 P(A|\bar{B})P(\bar{B}), \tag{4.19}$$

$$N_{\bar{A}B} = N_0 P(\bar{A}B) = N_0 P(\bar{A}|B)P(B), \tag{4.20}$$

$$N_{\bar{A}\bar{B}} = N_0 P(\bar{A}\bar{B}) = N_0 P(\bar{A}|\bar{B})P(\bar{B}) \tag{4.21}$$

If we plug the above expressions into the right-hand side of the single background solution, we have

$$\frac{N_{A\bar{B}}N_{\bar{A}B}}{N_{\bar{A}\bar{B}}} = \frac{N_0^2 P(A|\bar{B})P(\bar{B})P(\bar{A}|B)P(B)}{N_0 P(\bar{A}|\bar{B})P(\bar{B})} \tag{4.22}$$

When the correlation is small, we can use the following small quantities to correct the background prediction:

$$P(A|\bar{B}) = P(A|B) - \epsilon, \tag{4.23}$$

$$P(\bar{A}|\bar{B}) = P(\bar{A}|B) + \epsilon, \tag{4.24}$$

$$P(B|\bar{A}) = P(B|A) - \delta, \tag{4.25}$$

$$P(\bar{B}|\bar{A}) = P(\bar{B}|A) + \delta. \tag{4.26}$$

Then Equation 4.22 will become

$$\frac{N_{A\bar{B}}N_{\bar{A}B}}{N_{\bar{A}\bar{B}}} = \frac{N_0 P(\bar{A}|B)(P(A|B) - \epsilon)P(B)}{P(\bar{A}|B) + \epsilon}, \tag{4.27}$$

$$= \frac{N_0(P(A|B)P(B) - \epsilon P(B))}{1 + \frac{\epsilon}{P(\bar{A}|B)}}, \tag{4.28}$$

$$\approx (N_0(P(A|B)P(B) - \epsilon P(B))) \times(1 - \frac{\epsilon}{P(\bar{A}|B)} + \frac{\epsilon^2}{P(\bar{A}|B)^2} + \mathcal{O}(\epsilon^3)). \tag{4.29}$$

To second order of ϵ, we have

$$\frac{N_{A\bar{B}}N_{\bar{A}B}}{N_{\bar{A}\bar{B}}} = N_0 P(A|B)P(B) - \epsilon N_0(P(B) + \frac{P(A|B)P(B)}{P(\bar{A}|B)} + \epsilon^2 N_0(\frac{P(B)}{P(\bar{A}|B)} + \frac{P(A|B)P(B)}{P(\bar{A}|B)^2}). \tag{4.30}$$

Comparing the above expression with Equation 4.18, we have

$$N_{bkg} = \frac{N_{A\bar{B}}N_{\bar{A}B}}{N_{\bar{A}\bar{B}}} + \epsilon N_0 P(B)(1 + \frac{P(A|B)}{P(\bar{A}|B)}) \\ -\epsilon^2 N_0 \frac{P(B)}{P(\bar{A}|B)}(1 + \frac{P(A|B)}{P(\bar{A}|B)}). \quad (4.31)$$

If we assume the number of events in the signal box is small, then the first order correction term can be approximated without opening the signal box:

$$P(B) = \frac{N_{AB} + N_{\bar{A}B}}{N_0} \approx \frac{N_{\bar{A}B}}{N_0}, \quad (4.32)$$

$$\frac{P(A|B)}{P(\bar{A}|B)} = \frac{\frac{N_{AB}}{N_B}}{\frac{N_{\bar{A}B}}{N_B}} \approx \frac{N_{pred}}{N_{\bar{A}B}} \quad (4.33)$$

$$C_\epsilon = \epsilon N_{\bar{A}B}(1 + \frac{N_{pred}}{N_{\bar{A}B}}). \quad (4.34)$$

4.3 Background Estimation

The signal box was chosen to be a box in the three dimensional P_T-Mass-Z space with P_T between 0.1GeV/c and 0.2GeV/c, decay z vertex between 300cm and 500cm and invariant mass between 0.268GeV and 0.45GeV. The lower bound on the invariant mass is approximately twice the invariant mass of π^0 and the upper bound was chosen to avoid the mass peak of $K_L^0 \to \pi^0\pi^0$. The lower bound on P_T was chosen to avoid too much overlap with $K_L^0 \to 3\pi^0$ background and the upper bound was chosen based on the maximum P_T in $K_L^0 \to \pi^0\pi^0\nu\bar{\nu}$ MC. The lower bound on decay z vertex is downstream of CC02 and the upper bound is upstream of CV and CsI.

Because Run II used the beryllium (Be) absorber to reduce the beam neutrons and secured the membrane separating the vacuum and other detectors, neutron related

backgrounds become unimportant. There is no significant charged decay mode that can result in four photons in the final state. Because our signal box was chosen to avoid the mass peak of $K_L^0 \to \pi^0\pi^0$, it is negligible. Therefore, the dominant background source in Run II is $K_L^0 \to 3\pi^0$ with only four photon clusters identified in the final state.

Since π^0 decays into two photons with branching ratio 98.8%, normally there are six photons in the final state. There are two causes for photons not being identified. First, there can be photon inefficiency. The photon can escape through a crack or does not interact with the detector or interacts through photo-nuclear effect and does not the right timing. Second, there can be photon fusion, where two photons hit very close positions and are identified as one photon. Therefore, there are three ways $K_L^0 \to 3\pi^0$ can result in only four photons in the final state, two missing photons, one missing photon and one fusion, two fusion. Those three ways can be thought of as three background sources. We chose to put fusion neural-net cut in the setup cuts to eliminate most of the fusion events. Thus $K_L^0 \to 3\pi^0$ with two missing photons is the dominant background source.

4.3.1 Application of Bifurcation Method

The background estimation follows the bifurcation method. The setup cuts, cuts A and B are listed in Table 4.1. Cuts A are all photon veto cuts. Cuts B are all kinematic cuts, including photon quality cuts. CsI veto cut has features of both photon veto cuts and kinematic cuts. Therefore, it is included in setup cuts to reduce correlation. The kinematic cuts used for $K_L^0 \to \pi^0\pi^0\nu\bar{\nu}$ are described in Table 4.2.

In order to check how well the bifurcation method works, we also looked at a few

Setup cuts	Fusion Neural Network, Gamma Fiducial, CsI Veto, BA Veto
A	CC00, CC02, CC03, CC04(calorimeter), CC05(calorimeter), CC06, CC07, Front Barrel, Main Barrel, Sandwich Counter
B	z χ^2, TDI, RMS, Gamma Energy Ratio, EDI, Gamma Energy

Table 4.1: Organization of the cuts.

Cut	Values	Comments
Photon Energy Min.	150 MeV	
Photon CsI Hit Position	$17.5 < r < 88$ cm	The inner dimension forms a square around the beam pipe, the outer is radial.
Photon Fusion Neural Network Min.	0.75	
Best χ^2 Max.	0.5	
2nd Best χ^2 Min.	12.5	
Gamma RMS Max.	6.0	
Gamma Energy Ratio Min.	0.8	
EDI Min.	0.8	
TDI Max.	2.0	

Table 4.2: Kinematic Cuts for $K_L^0 \to \pi^0\pi^0\nu\bar{\nu}$.

regions surrounding the signal box. The Low P_T region and High P_T region are the regions with the same z and invariant mass range as the signal box and have P_T from 0.0GeV/c to 0.1GeV/c and 0.2GeV/c to 0.3GeV/c respectively. The Low Z and High Z regions share the same P_T and invariant mass bounds as the signal box and have Z from 250 cm to 300 cm and 500 cm to 550 cm respectively. The High Mass region has the same P_T and Z bounds as the signal box and has invariant mass between 0.45GeV and 0.55GeV. Table 4.3 shows the measurement and prediction in various regions. The ϵ computed using the Low P_T region is -0.000431. In all regions (except Low Z), measurement and prediction matched within two sigma. So the correlation

is negligible and we think there is no need to include correlation correction in the background prediction.

Region	N_0	$N_{A\bar{B}}$	$N_{\bar{A}B}$	$N_{\bar{A}\bar{B}}$	N_{AB}	N_{pred}
Signal box	unknown	2	247	1901	unknown	0.26 ± 0.18
Low P_T	109892	982	10663	98145	102	106.69 ± 3.57
High P_T	37	1	5	31	0	0.16 ± 0.18
High Mass	945	10	133	800	2	1.66 ± 0.55
Low Z	92	9	10	70	3	1.29 ± 0.61
High Z	510	4	12	494	0	0.10 ± 0.06

Table 4.3: Measurement and prediction in various regions.In the signal box, N_0 and N_{AB} are unknown at this stage because it is a blind analysis. The errors in background prediction are only statistical.

4.3.2 Correction from Multiple Background Sources

As mentioned before, $K_L^0 \to 3\pi^0$ can form backgrounds in three ways, two missing photons (zero fusion), one missing photon and one fusion, two fusion. Those three ways can be thought of as three background sources. We will estimate the correction from multiple background sources following Equation 4.17. Let N_1, N_2 and N_3 be the number of background events that pass the setup cuts for the zero fusion, one fusion and two fusion background sources respectively. Let $P_i(A)$ and $P_i(B)$ be the passing probabilities of each background source. We will use $K_L^0 \to 3\pi^0$ MC to estimate those quantities. The setup cuts are applied to $K_L^0 \to 3\pi^0$ MC with four photon clusters in the final state. When the distance between the CsI hit positions of two photons is less than a certain threshold ($7cm$, $10.5cm$ or $14cm$), they are classified as fusion. Table 4.4 shows the percentage of the three background sources using different photon separation thresholds.

Minimum Separation	0 fusion	1 fusion	2 fusion
7 cm	99.73%	0.23%	0.04%
10.5 cm	99.41%	0.49%	0.09%
14 cm	99.00%	0.80%	0.20%

Table 4.4: Percentages of the three background sources after the setup cuts are applied.

Most of the CsI crystals are $7cm \times 7cm$, so $10.5cm$ should be an appropriate threshold for fusion. So I used $10.5cm$ as the threshold to estimate the passing probabilities of the three background sources. Results are shown in Table 4.5.

Cuts	0 fusion	1 fusion	2 fusion
P(A)	0.00308	0.0449	0.110
P(B)	0.139	0.177	0.116

Table 4.5: Passing probabilities of the three background sources for cuts A and B.

In Table 4.3, for signal box $N_{A\bar{B}} + N_{A\bar{B}} + N_{\bar{A}\bar{B}} = 2150$. If we assume N_{AB} is very small, we can approximate the total number of background events (N_0) by $N_{A\bar{B}} + N_{A\bar{B}} + N_{\bar{A}\bar{B}} = 2150$. Then using the percentages in Table 4.4, we can estimate N_1, N_2 and N_3 as the following:

$$N_1 = 2150 \times 99.41\% = 2137 \tag{4.35}$$

$$N_2 = 2150 \times 0.49\% = 10.6 \tag{4.36}$$

$$N_3 = 2150 \times 0.09\% = 2.0 \tag{4.37}$$

Then plugging the above estimates and the passing probabilities in Table 4.5 into Equation 4.17, we can get the correction from multiple background sources. The results are given in Table 4.6.

The correction from multiple background sources is treated as a systematic error.

	Correction
N_1 and N_2	0.019
N_1 and N_3	-0.0057
N_2 and N_3	-4.5×10^{-5}
Total Correction	0.013

Table 4.6: Background prediction correction from multiple background sources.

Thus the final background estimation is $0.26 \pm 0.18_{stat} \pm 0.01_{syst}$.

CHAPTER 5

CONCLUSIONS

5.1 Acceptance and S.E.S

The acceptance of $K_L^0 \to \pi^0\pi^0\nu\bar{\nu}$ was calculated by applying all analysis cuts to $K_L^0 \to \pi^0\pi^0\nu\bar{\nu}$ MC. Because there is no significant charged mode that can form background, charge veto cuts are only applied at the online veto level. Both $K_L^0 \to \pi^0\pi^0\nu\bar{\nu}$ MC with a pure phase space decay and $K_L^0 \to \pi^0\pi^0\nu\bar{\nu}$ MC with a form factor were used. The pure phase space decay MC gave the acceptance as $(3.79 \pm 0.06) \times 10^{-4}$ and the MC with a form factor gave the acceptance as $(3.77 \pm 0.06) \times 10^{-4}$, which are pretty close. The acceptance from the pure phase space decay MC is used for this analysis. The systematic error in the acceptance is hard to estimate because we don't have a large amount of well-reconstructed $K_L^0 \to \pi^0\pi^0\nu\bar{\nu}$ events in data. So we used the systematic error in the normalization mode $K_L^0 \to \pi^0\pi^0$, 4.7%, as the estimate of the systematic error in acceptance. So the final acceptance is $(3.79 \pm 0.06_{stat} \pm 0.18_{syst}) \times 10^{-4}$.

The Single Event Sensitivity is

$$\begin{aligned} S.E.S. &= \frac{1}{Acceptance \times Flux} \\ &= (4.70 \pm 0.35) \times 10^{-7} \end{aligned} \tag{5.1}$$

5.2 Opening Box and Final Result

After opening the box, we observed zero event after applying all the analysis cuts. Figure 5.1 and Figure 5.2 show the opened box.

Using Poisson statistics, we can set the upper limit on the branching ratio at the

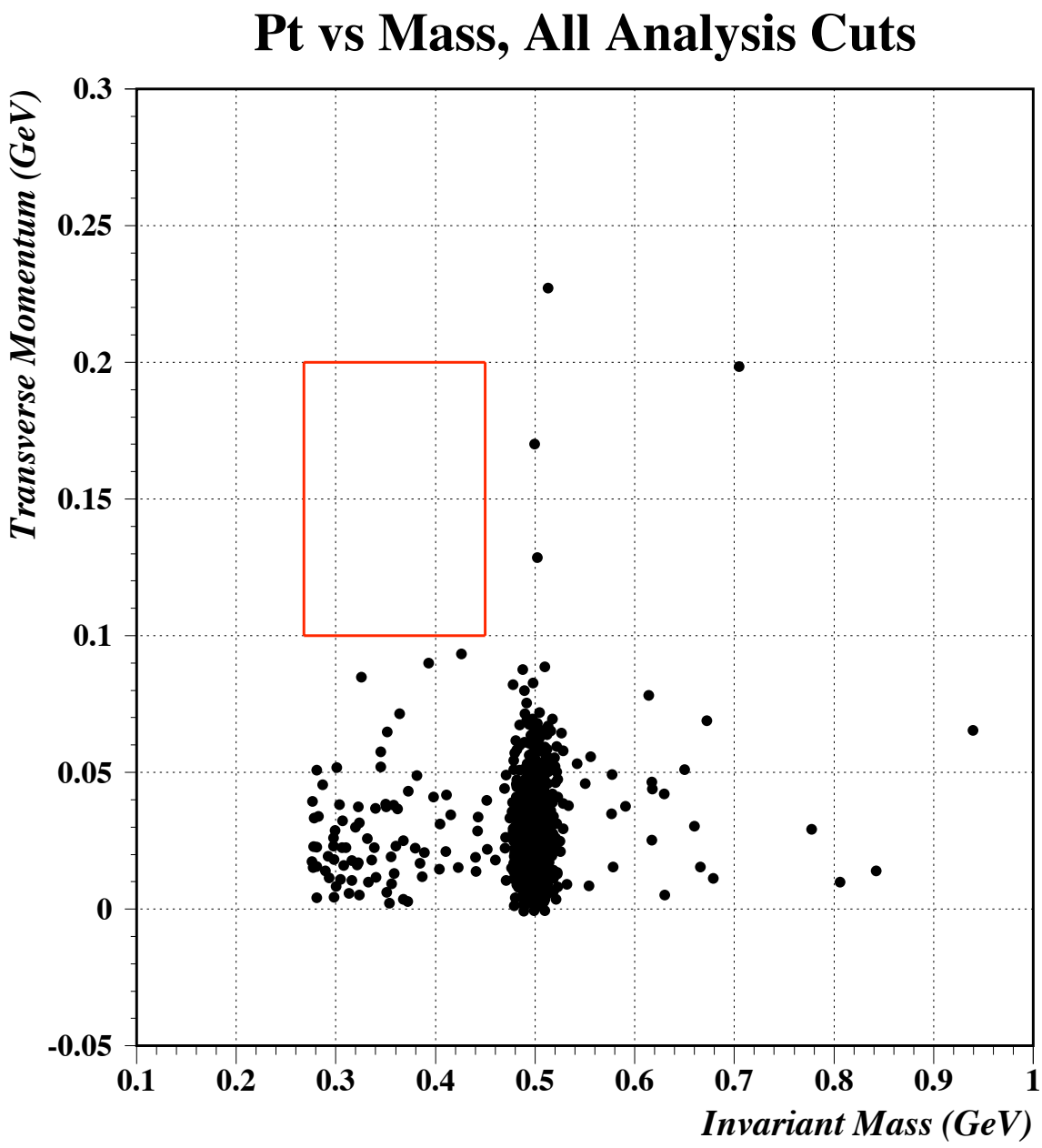

Figure 5.1: The four-cluster data with all the analysis cuts applied. Only events with decay z vertex between 300cm and 500cm are shown. The red box shows the signal box.

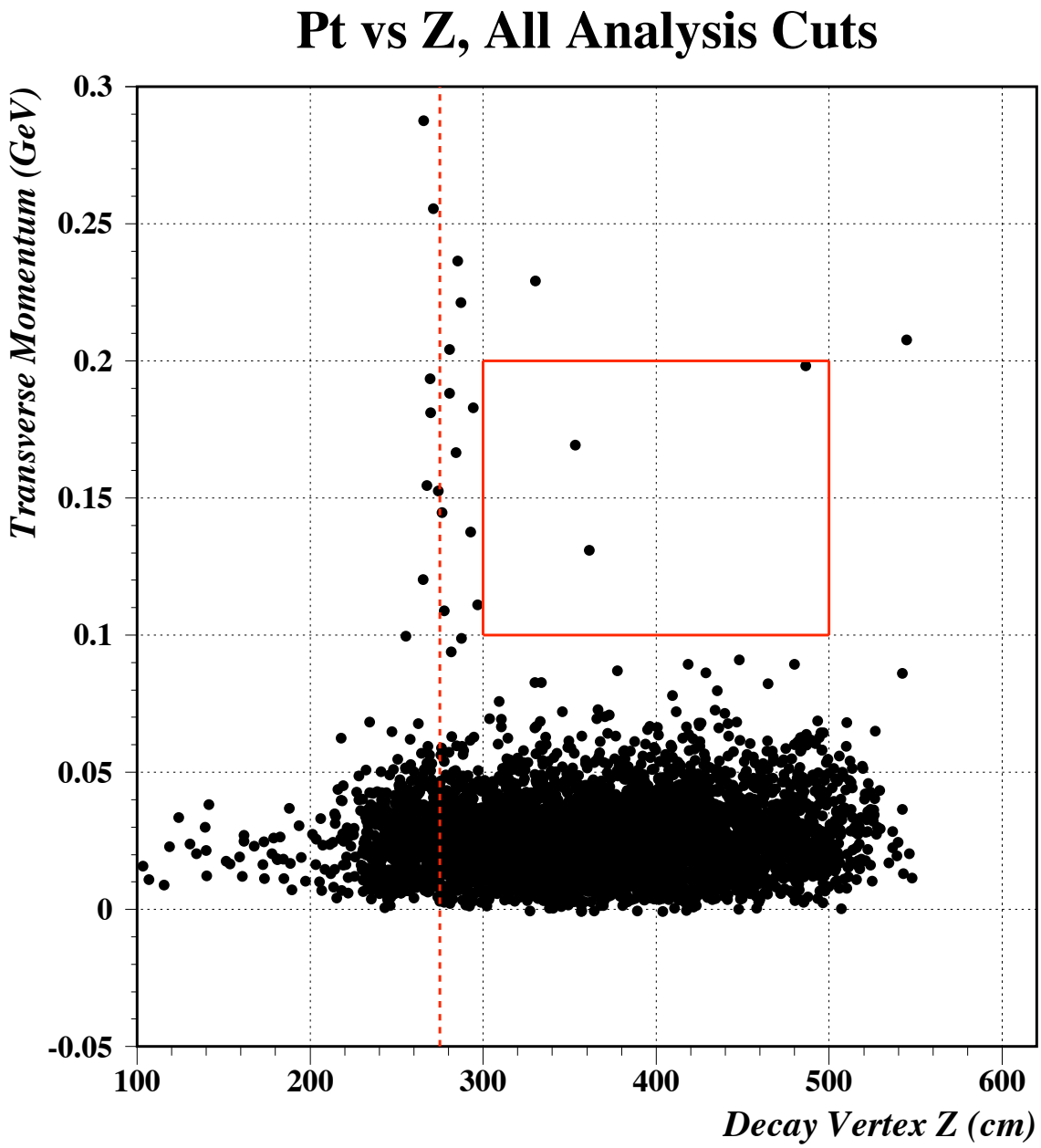

Figure 5.2: The four-cluster data with all the analysis cuts applied. The red box shows the signal box. The red vertical line shows the position of the end of CC02.

90% confidence level:

$$Br(K_L^0 \to \pi^0\pi^0\nu\bar{\nu}) < 2.3 \times 4.70 \times 10^{-7} = 1.08 \times 10^{-6}. \tag{5.2}$$

Using the formula in [22], we can take the uncertainty on the flux and acceptance into account. Then the upper limit at the 90% confidence level is

$$\begin{aligned} Br(K_L^0 \to \pi^0\pi^0\nu\bar{\nu}) &< 2.3 \times (1 + 2.3/2 \times (\sigma_{\text{S.E.S.}}/\text{S.E.S.})^2) \times \text{S.E.S.} \\ &= 1.09 \times 10^{-6}. \end{aligned} \tag{5.3}$$

5.3 Future Prospect

The E391a collaboration is planning a new experiment, E14 also known as Koto, at JPARC in Tokai, Japan. The new experiment is expected to start data taking in one and a half years. E14 will use smaller crystals for the CsI array, which can increase the position resolution and background rejection power. The crystals will also be longer to contain the full electromagnetic shower. The flux will be larger than E391a. The newly developed ADC boards will also increase the timing resolution. Such improvements should allow analysis of more data without background limitation.

REFERENCES

[1] L.S. Littenberg and G. Valencia. The decays $K \to \pi\pi\nu\bar{\nu}$ within the standard model. *Phys. Lett. B*, 385(379), 1996.

[2] C.W. Chiang and F.J. Gilman. $K_{L,S} \to \pi\pi\nu\bar{\nu}$ decays within and beyond the standard model. *Physical Review D*, 62:094026, 2000.

[3] G. Buchalla, A. Buras and M. Harlander. CP-conserving and -violating contributions to $K_L \to \pi^+\pi^-\nu\bar{\nu}$. *Nucl. Phys. B*, 349:1, 1991.

[4] J. Nix et al. First search for $K_L \to \pi^0\pi^0\nu\bar{\nu}$. *Phys. Rev. D (RC)*, 76(011101(R)), 2007.

[5] T. D. Lee and C. N. Yang. *Physical Review*, 104(254), 1956.

[6] C. S. Wu et al. Experimental Test of Parity Conservation in Beta Decay. *Physical Review*, 105, 1957.

[7] J. H. Christenson, J. W. Cronin, V. L. Fitch, and R. Turlay. Evidence for the 2π decay of the K_2^0 meson. *Physical Review Letters*, 13(4), 1964.

[8] A. J. Buras. CP Violation and Rare Decays of K and B Mesons. hep-ph/9905437, 1999.

[9] Nicola Cabibbo. Unitary Symmetry and Leptonic Decays. 10(12), 1963.

[10] M. Kobayashi and T. Maskawa. CP Violation in the Renormalizable Theory of Weak Interactions. *Progress of Theoretical Physics*, 49(2), 1973.

[11] L. Wolfenstein. Parametrization of the Kobayashi-Maskawa Matrix. *Physical Review Letters*, 51(21), 1983.

[12] S. L. Glashow, J. Iliopoulos, and L. Maiani. Weak Interactions with Lepton-Hadron Symmetry. *Phys. Rev. D*, 2(7):1285–1292, Oct 1970.

[13] H. Watanabe et al. Neutral beam line to study $K_L^0 \to \pi^0\nu\bar{\nu}$ decay at the KEK 12-GeV proton synchrotron. *Nuclear Instruments and Methods in Physics Research A*, 545:542–553, 2005.

[14] K. Sakashita. *Search for the decay* $K_L^0 \to \pi^0\nu\bar{\nu}$. PhD thesis, Osaka University, 2006.

[15] J. D. Nix. Study of the Necessity of Collar Counters 1 and 4. Internal Memo, 2001.

[16] H. Watanabe. PhD thesis, Saga University, 2002.

[17] M. Doroshenko et al. Undoped CsI calorimeter for the $K_L^0 \to \pi^0\nu\bar{\nu}$ experiment at KEK-PS. *Nuclear Instruments and Methods in Physics Research A*, 545:278–295, 2005.

[18] K. F. "Jack" Chen. CsI Calibration Using $K_L^0 \to 3\pi^0$ Decays. Internal Memo, 2005.

[19] G. N. Perdue. *Search for the rare decay* $K \to \pi^0\nu\bar{\nu}$. PhD thesis, The University of Chicago, 2008.

[20] S. Adler et al. Evidence for the Decay $K^+ \to \pi^+\nu\bar{\nu}$. *Phys. Rev. Lett.*, 79:2204, 1997.

[21] J. D. Nix. *First Search for* $K \to \pi^0\pi^0\nu\bar{\nu}$ *and* $K \to \pi^0\pi^0 P$. PhD thesis, The University of Chicago, 2007.

[22] R. Cousins and V. Highland. Incorporating systematic uncertainties into an upper limit. *Nuclear Instruments and Methods in Physics Research A*, 320:331–335, 1992.